This is to certify that the

thesis entitled

Adhesion, Processing and Interfacial Properties of
Preceramic Polymer Coatings on Carbon Fibers

presented by

Tauseef Muhammad Chaudhry

has been accepted towards fulfillment
of the requirements for

M.S. degree in Materials Science

Lawrence T. Drzal
Major professor

Date September 22, 1995

ADHESION, PROCESSING AND INTERFACIAL PROPERTIES OF PRECERAMIC POLYMER COATINGS ON CARBON FIBERS

By

Tauseef Muhammad Chaudhry

A THESIS

Submitted to

Michigan State University

in partial fulfillment of the requirements

for the degree of

MASTER OF SCIENCE

Department of Materials Science and Mechanics

1995

ABSTRACT

ADHESION, PROCESSING AND INTERFACIAL PROPERTIES OF PRECERAMIC POLYMER COATINGS ON CARBON FIBERS

By

Tauseef Muhammad Chaudhry

Preceramic inorganic polymer coatings are applied to graphite fibers by dip coating tows of fibers into hexane solution of the silsesquioxane terpolymer $-[\mathrm{MeHSiO}]_{0.1}[\mathrm{MeSi(OnPr)O}]_{0.2}[\mathrm{MeSi(O)}_{1.5}]_{0.7}-$ to form silsesquioxane coatings typically 0.1 μm thick. The coatings are then pretreated by heating in nitrogen to high temperatures (200 °C increments to 1000 °C). The amorphous polymeric coatings were shown to convert to amorphous silicon oxycarbide coatings on heating to temperatures above 600 °C. Single carbon fibers coated with silicon oxycarbide coatings were pyrolyzed and then encapsulated in a transparent epoxy matrix so that stress could be applied and the adhesion and fracture behavior of the coatings could be observed. The properties and adhesion of the coatings to the carbon fibers change with the degree of pyrolysis. Initially the adhesion is low and a mixed fiber-coating and coating-matrix interfacial failure is observed. After thermal processing to 800 °C and above, a significant increase in adhesion with circumferential cracks in the coating are detected and the fiber-coating interfacial failure is observed. The interface is observed as intact in the case of the unstrained samples, whereas it is disrupted in the samples subjected to uniaxial tension. A non-linear axisymmetric finite element model of this single fiber coated with material having properties varying in a manner similar to the coating was used to analyze the mechanical state of stress in the coating and at the interface.

DEDICATED

TO

Dr. Muhammad Iqbal, The Poet-Philosopher of the 20th Century

And

Professor Annemarie Schimmel, The Orientalist of Present Time

Who Profoundly Moved and Inspired Me.

ACKNOWLEDGMENTS

I thank Allah, the Creator and the Cherisher of the universe for giving me the ability to complete this work. I am thankful to my parents who always stressed the importance of education as well as personal character.

My heart felt thanks are due to my adviser Professor Lawrence T. Drzal for giving me the opportunity and for his guidance and encouragement towards understanding of things and towards purification of thought.

I would like to thank the friendly staff of Composite Materials and Structures Center (CMSC). My thanks are due to Mike Rich and Brian Rook for their help and suggestions in operating the equipments at CMSC. I am especially thankful to Dr. Henjen Ho for the helpful and informative discussions on the finite element model he developed and for his friendship. I thank Dan Hook for his help in surface analysis. My thanks go to Dr. Steve Rozeveld for the help in environmental scanning electron microscopy.

I am indebted to Dr. John Heckman of the Center for Electron Optics for his assistance in the ultramicrotomy and transmission electron microscopy.

Finally, I would like to thank all my friends here at the Michigan State University for their support and friendship.

TABLE OF CONTENTS

LIST OF TABLES

LIST OF FIGURES

CHAPTER 1

INTRODUCTION

The long term goals of the work are (1) to develop methods of modifying fiber surfaces with well-defined ceramic coatings made using preceramic polymers, (2) to identify (define) the ceramic coating and coating-fiber interface failure mechanisms at both the atomic and nanostructural levels, and (3) to use the data obtained to identify the fundamental material, processing and adhesion factors that control interface properties in order to have the maximum benefit of these coatings on Metal Matrix Composite (MMC) and Ceramic Matrix Composite (CMC) mechanical properties.

The first step in this process has been to establish a benchmark interface and to clearly define its attendant properties. The characteristics of the benchmark interface coating material, silicon oxycarbide, SiO_xC_y or black glass have been studied **[1]**. SiO_xC_y was chosen because (1) SiO_xC_y is amorphous, (2) it is possible to prepare very well-defined materials, where the chemistry and the evolution of the material with time and temperature are known in detail, and (3) SiO_xC_y is a matrix material used in commercial composites. Results were presented which provided the experimental methods and the characterization of the processable inorganic polymer precursor, $-[MeHSiO]_{0.1}[MeSi(OnPr)O]_{0.2}[MeSi(O)_{1.5}]_{0.7}-$. In addition, it has been shown that these coatings are effective in increasing the oxidation resistance of the carbon fibers themselves. Most of the associated changes in chemistry and oxidation resistance improvement with conversion from inorganic polymer to ceramic coating take place in the temperature regime from 600 °C to 1000 °C. During this process of conversion from inorganic polymer to ceramic, the coating converts to an amorphous silicon oxycarbide, there is a volumetric shrinkage associated with this conversion and the coating has the properties of a ceramic instead of a polymer.

To determine whether the preceramic inorganic polymer coating can provide not only the thermal oxidative protection during both processing and use in MMCs or CMCs but also the appropriate composite properties, it is desirable to know how and at what point in the thermal processing cycle the coating-carbon fiber interface undergoes changes that affect the interfacial adhesion and failure mode. Also, it is important to identify the locus of interfacial failure i.e. between fiber and coating or between coating and matrix. This work is directed at determining the interfacial changes and the locus of failure in order to optimize both the coating chemistry and the conversion process.

Intense efforts to develop superior fiber-reinforced composites with exceptional mechanical properties and long-term structural reliability have been undertaken during the past decade. A considerable part of this effort has focused on developing basic principles concerned with how stress from an applied load is distributed (1) within the composite matrix materials; (2) through the fibers themselves and especially, (3) at the fiber-matrix interface where primary load transfer occurs.

Much of the work on load transfer at the interface has targeted the development of fundamental structure-property relationships from fiber-matrix interface behavior. Several groups have explored approaches based purely on mechanics with some basic assumptions concerning adhesion of the fiber to the matrix [2-4]. Others have considered the idea that load transfer occurs solely at the interface via the chemical links at that interface [5,6]. Both methods fall short of accurately predicting composite performance. It is now accepted that coupling these approaches to structure-property relationships provides a more accurate method of predicting composite behavior [7,8]. Recent studies show that small changes in the level of adhesion and the properties of the material in the interphase region can have profound effects on composite mechanical properties [9,10].

In large part, these relationships were developed for rigid, reinforcing fibers in relatively compliant matrix materials, polymers. Less effort has been directed towards developing interfacial structure-property relationships for CMCs and MMCs. This problem derives from the technical difficulties inherent in reproducibly processing CMCs and MMCs. Additional problems arise because it is much more difficult to characterize interface properties in MMCs and CMCs by comparison with polymer composite systems. As a consequence, detailed modeling studies on load transmission across the fiber-matrix interfaces in CMCs and MMCs have not been forthcoming. Furthermore, little effort has been made to develop general methods of tailoring fiber-matrix interfaces in these materials to optimize performance as a function of application. The continued and growing importance of fiber-reinforced CMCs and MMCs in both defense and industrial applications requires that these problems be addressed and provides motivation for the work reported here.

CHAPTER 2

BACKGROUND

To develop detailed structure-processing-property relationships, one must identify key criteria that can be used; first to assess a given interface, and then to justify any resulting conclusions concerning long term mechanical properties. At the macroscopic level, we must be concerned with interfacial failure mechanisms both within the fiber coating and at the coating-matrix interface, either during processing or in use. At the atomic scale, we must be concerned about interface chemistry.

Establishment of structure-property relationships between fiber-matrix adhesion and composite behavior depends on both the level of adhesion and the interfacial failure mode if composite properties are to be optimized for strength and toughness. High strength interfaces by themselves produce a low degree of composite toughness by allowing cracks to propagate across fibers in a catastrophic manner. Very low values of adhesion produce an increase in composite toughness but at the expense of static mechanical properties. If a ceramic coating is placed at the interphase, the brittleness and fracture behavior of the coating during composite processing and subsequent usage can reduce the fiber strength and composite properties. Understanding of the fiber surface chemistry, the development of interfacial bonds, the interdiffusion and resulting interphase property gradient are all necessary information required before optimum interfaces can be designed.

At the atomic level, quantification of the elemental composition and identification of particular bonding arrangements present both at the fiber surface and in the interfacial material, especially as both evolve with processing, may provide insight into nanostructural events, e.g. failure modes. Auger, XPS and FTIR spectroscopic methods can be used to quantify the structural and compositional changes that occur with processing which can be used as the basis to quantify the factors that affect adhesion of an applied coating or matrix.

Total encapsulation of the fiber in a polymer matrix has the advantages of both placing the fiber under the same state of stress encountered in a CMC or MMC and also allowing the interface to be interrogated and observed with methods found useful with the fiber-matrix interphase in composite materials.

2.1 COMPOSITE INTERPHASE

The juncture that exists when the matrix and fiber come together in composite materials is a three dimensional interphase rather than a two dimensional interface/boundary. The complexity of this region can best be illustrated with the use of a schematic model which allows the potential important characteristics of this region to be identified as shown in **Figure 2.1**.

The interphase exists from some point in the fiber where the local properties begin to change from the fiber bulk properties through the interface into the matrix where the

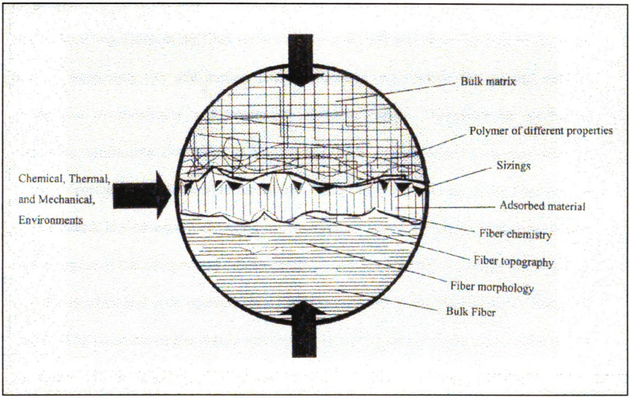

Figure 2.1 Schematic representation of fiber-matrix interphase in a composite material **[12]**.

local properties again equal the bulk properties. Components of this region can be identified. The fiber may have morphological variations near the fiber surface which are not present in the bulk of the fiber. The surface area of the fiber can be much greater than its geometrical value because of pores or cracks present on the surface. The atomic and molecular composition of the fiber surface can be quite different from the bulk of the fiber. Surface treatments can add surface chemical groups and remove the original surface giving rise to chemically and structurally different region. Exposure to air before composite processing can result in the adsorption of components which may alter or eliminate certain beneficial surface reactivity. Thermodynamic wetting of the fiber surface by the matrix is a necessary condition for fiber-matrix adhesion and is determined by the free energies of the components. Both chemical and physical bonds exist at the interface and the number and type of each strongly influences the interaction between fiber and matrix. The structure of the matrix near the fiber surface can be influenced. Changes in reactivity due to adsorption of matrix components can alter the local morphology. Untreated matrix components and impurities can diffuse into the interphase region altering the local structure.

Each of these phenomena can vary in magnitude and can occur simultaneously in the interphase region. Depending on the system the interphase itself can extend from a few to a few hundred nanometers in depth. The structure of this region can have profound effects on the performance of the composite in terms of its mechanical strength, chemical and thermal durability. Likewise the exact nature of this region must be understood if accurate life prediction models are to be developed. A need for a multidisciplinary approach must be recognized because of the complexity of this region.

The complexity of the interphase region requires that a variety of characterization methods be applied to fully understand the chemical and physical nature of this region. The methods and the information which they provide are: (1) Surface Spectroscopies, i.e. atomic and molecular information about the reinforcement surface; (2) Thermal Desorption, the identification and quantification of the species able to volatilize at the interphase during fabrication; (3) Surface Energies, the thermodynamic quantities necessary to predict the wettability of the reinforcement surface and the interaction with the matrix; (4) Mechanical response of the interphase to environment or the interfacial shear strength; (5) Microtomy and Microscopy, i.e. the determination of the locus of failure in the interphase region.

Ceramic materials are known for their high temperature resistance with the drawback of low toughness and strength. Ceramic matrix composites are developed to give high strength, high toughness and better damage tolerance, and a lower variability of strength over monolithic ceramics. The fiber-matrix interface in fiber-reinforced ceramic matrix composites controls the mechanical behavior of these materials. An extremely strong bond does not allow for crack deflection or debonding at the fiber-matrix interface therefore a crack propagating in the matrix simply passes through the fibers undisturbed resulting in brittle fracture. Conversely, an extremely weak interface leads to a low matrix fracture stress and low ultimate strength, for as the composite is stressed, load is not transferred efficiently from the matrix to the fibers, thus the properties of the reinforcement are not utilized. Therefore, interfacial forces must be controlled to produce a composite material with good matrix failure stress and ultimate strength that also exhibits gradual composite failure through effective fiber pull-out. Coating the fiber with a suitable reinforcement can be used to control the interfacial forces.

Metal matrix composites are produced by two ways: molten metal processing and powder metallurgy. The former route is the most severe from the point of view of interfacial reactions because the liquid metal is very reactive to the fiber surface. Main elements that contribute to the role of interphase in metallic matrix composites are: (1) thermal residual stresses due to the mismatch in the thermal expansion coefficients of fiber and matrix, (2) chemical reaction between the fiber and matrix materials, (3) fiber surface characteristics that may include large asperities and/or a certain roughness amplitude, and (4) friction between the fiber and the matrix that may result in improved toughness due to energy dissipated in fiber bridging and pullout. Extensive interface reaction can result in degradation of the reinforcement, which is particularly a problem in continuous fiber reinforced metal matrix composites, and it can also result in a modification of the matrix metallurgy and properties. A protective coating to provide thermo-oxidative stability to the reinforcing fiber can help prevent degradation of the reinforcement by controlling kinetics and diffusion.

2.2 THEORIES OF ADHESION

Bonding at an interface is due to adhesion between fiber and matrix. Adhesion can be attributed to five main mechanisms which can occur at the interface either in isolation or in combination to produce the bond. These mechanisms are briefly discussed below.

2.2.1 Adsorption and Wetting

When two electrically neutral surfaces are brought sufficiently close together there is a physical attraction which is best understood by considering the wetting of solid surfaces by liquids. In the case of two solids being brought together the surface roughness on a micro and atomic scale prevents the surfaces coming into contact except at isolated points. In addition the surfaces are usually contaminated. Even if the contamination is removed, and strong adhesion occurs at the contact points, the adhesion averaged over the whole surface will be weak. For effective wetting of a fiber surface the liquid resin must cover every hill and valley of the surface to displace all the air. Weak boundary layers must be avoided also.

Wetting can be understood in terms of two simple equations. The Dupre equation for the thermodynamic work of adhesion, W_A of a liquid to a solid states that

$$W_A = \gamma_1 + \gamma_2 + \gamma_{12} \qquad (2.1)$$

where γ_1 and γ_2 are the surface free energies of the liquid and solid respectively and γ_{12} is the free energy of the liquid-solid interface. This equation can be related to the physical situation of a liquid drop on a solid surface by using the Young equation. When the forces are resolved in the horizontal direction at a point where the liquid touches the solid as well as the vapor, then the Young's equation states

$$\gamma_{SV} = \gamma_{SL} + \gamma_{LV} \cos\theta \tag{2.2}$$

where γ_{SV}, γ_{SL} and γ_{LV} are the surface free energies, or surface tensions of the solid-vapor, solid-liquid and liquid-vapor interfaces respectively, and θ is the contact angle. For spontaneous wetting to occur $\theta = 0^{\circ}$. Zisman introduced the concept of critical surface tension of wetting γ_C such that only liquids with $\gamma_{LV} < \gamma_C$ will spontaneously spread on the solid. This is a useful parameter in considering the wetting of fibers by resins.

A value for W_A can be obtained by combining equations (2.1) and (2.2) and putting $\gamma_1 = \gamma_{SV}$, $\gamma_2 = \gamma_{LV}$ and $\gamma_{LV} = \gamma_{SL}$, namely,

$$W_A = \gamma_{SV} + \gamma_{LV} - \gamma_{SL} \tag{2.3}$$

W_A represents a physical bond resulting from highly localized intermolecular dispersion forces which, in the ideal situation, can give very strong adhesion between resin and carbon or glass fibers. However, this strong physical bond is usually not achieved (1) because the fiber surface is contaminated so that the effective surface energy is much smaller than that of the base solid, (2) because of the presence of entrapped air and other gases at the solid surface, and (3) because of the occurrence of large shrinkage stresses during the curing process which leads to displacements at the surface which can not be healed.

2.2.2 Interdiffusion

It is possible to form a bond between two polymer surfaces by the interdiffusion of the polymer molecules on one surface into the molecular network of the other surface.

The bond strength will depend on the amount of molecular entanglement and the number of molecules involved. Interdiffusion may be promoted by the presence of solvents and plasticising agents and the amount of diffusion will depend on the molecular conformation and constituents involved and the ease of molecular motion. Interdiffusion of the preceramic polymer coating with the polymer matrix may account in part for the bonding achieved when fibers are pre-coated before incorporating into the matrix.

2.2.3 Electrostatic Attraction

Forces of attraction occur between two surfaces when one surface carries a net positive charge and the other surface a net negative charge. The strength of the interface will depend on the charge density and the potential difference between the two surfaces. Although electrostatic attraction is unlikely to make a major contribution to the final bond strength of fiber-matrix composites, it could well have an important role in the way that coupling agents are laid down on the surface of glass fibers.

2.2.4 Chemical Bonding

This is of particular interest for fiber composite materials because it offers the main explanation for the strength of the bond between fiber and matrix. A chemical bond is formed between a chemical group on the fiber surface and a compatible chemical group in the matrix. The strength of the bond depends on the number and type of bonds and interface failure must involve bond breakage. The processes of bond formation and breakage are in some form of thermally activated dynamic equilibrium.

2.2.5 Mechanical Adhesion

Some bonding may occur purely by the mechanical interlocking of two surfaces. A resin which completely wets the fiber surface follows every detail of that surface. The strength of this interface in tension is unlikely to be high unless there are a large number of re-entrant angles on the fiber surface. The strength in shear may be very significant and depends on the degree of roughness. A quite separate factor which also relates to the roughness of the fiber surface is the potential for an increased bond strength, for example, chemical bonding because of the larger surface area which is available.

In addition to the simple geometrical aspects of mechanical adhesion, there are many internal stresses in a composite material which develop during processing operations and mechanical testing which affect the apparent strength of the fiber-matrix bond. Thus, for example, resin shrinkage during curing of thermosetting polymers and differential thermal expansion of the matrix and fibers can produce tensile, compressive and shear stresses at the interface depending on the geometry of the fibers and the component.

2.3 ADHESION TESTS

The level of adhesion between fiber and matrix affects the mechanical properties of a composite. Several methods have been proposed to relate structure and property to composite fiber-matrix interfacial behavior [9,11,12]. The fibers are considered to be the load bearing constituent and the mechanism of load transfer at the fiber-matrix interphase plays a major role in the mechanical and physical properties of the composite. In this study, the Single Fiber Fragmentation and the Microindentation techniques are used for the adhesion characterization. A description of these fiber-matrix adhesion tests is given below.

2.3.1 Single Fiber Fragmentation Test

This technique was originally used by Kelly and Tyson **[13]**, who observed a multiple fiber fracturing phenomenon on application of a tensile force in a system consisting of a low concentration of brittle fibers embedded in a copper matrix. Drzal et al. used graphite fiber/epoxy system to study the interfacial shear stress transfer mechanism upon application of a tensile load to the single fiber coupon **[7,14,15,16]**.

In this method a fiber is embedded in a matrix material such that the strain to failure of the matrix is at least three times higher than that of the fiber. An axial stress induced in the fiber by interfacial shear stress increases from the fiber ends until the fiber fracture strength σ_f is reached as shown in the **Figure 2.2**. At that point, the fiber fractures at some site where the fiber stress is at a maximum, depending on fiber defect distribution and probability. Continued application of stress to the specimen will result in repetition of this fragmentation process until all remaining fiber lengths become so short that the shear stress transfer along their lengths can no longer build up enough tensile stresses to cause any further failures with increasing strain. This maximum final fragmentation length of the fiber is referred to as the critical length l_c. The equilibrium of forces gives

$$(\sigma_f + d\,\sigma_f)\,\pi\,r^2 = \sigma_f\,\pi\,r^2 + 2\,\pi\,r\,\tau\,dx$$

$$d\,\sigma_f = (2\,\tau / r)\,dx$$

$$\int_0^x d\sigma_f = \int_0^x (2\,\tau / r)\,dx$$

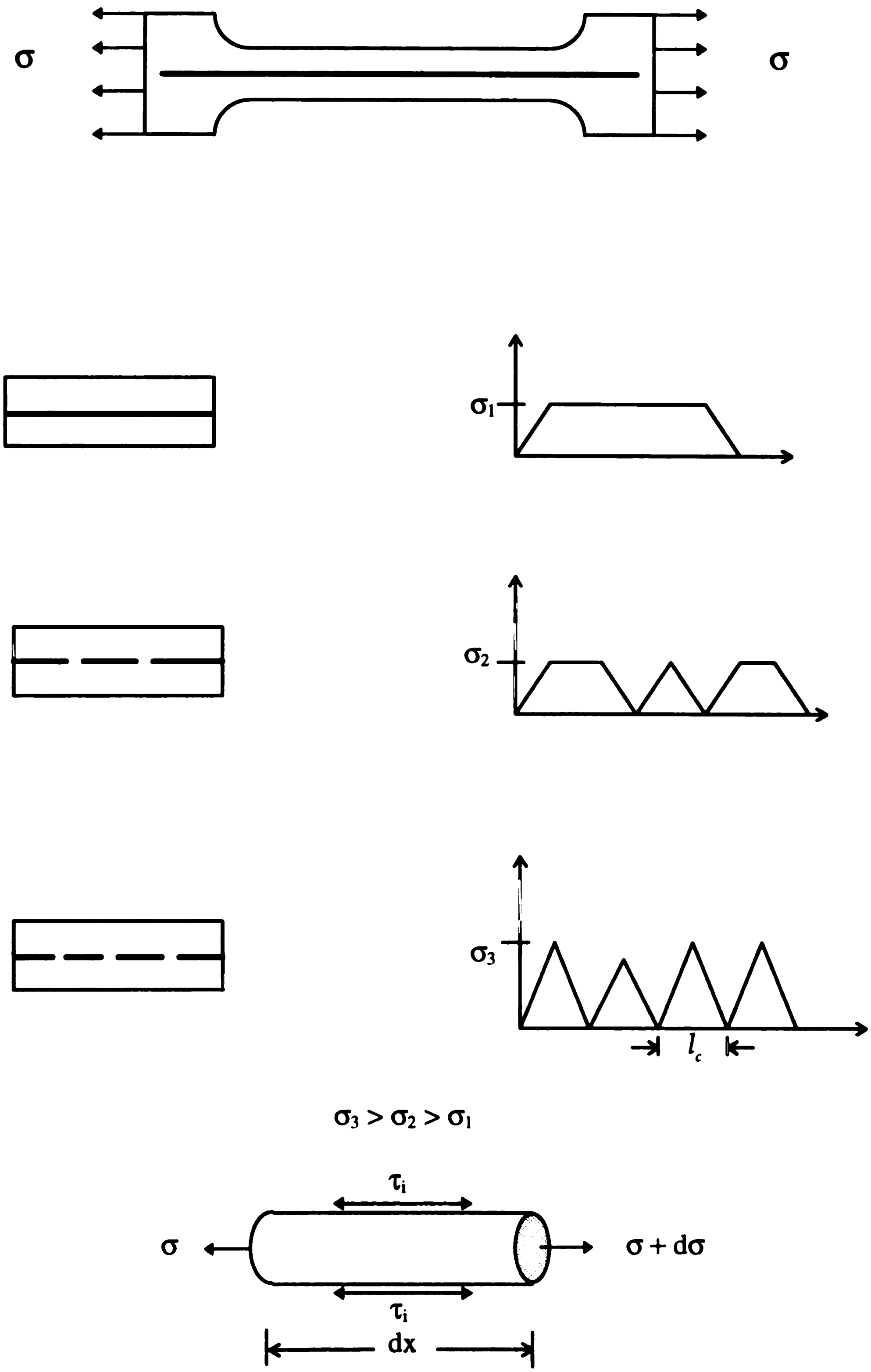

Figure 2.2 Schematic representation of the single fiber fragmentation process.

$$\sigma_{fx} - \sigma_{f0} = (2/r) \int_0^x \tau \, dx$$

Where r is the radius of the fiber and σ_{f0} is the stress at the fiber end which is equal to zero as the fiber end can not take stress and σ_{fx} is equal to σ_f. If the matrix surrounding the fiber is a perfectly plastic matrix, the shear stress τ at the interface can be considered to be constant along the short fiber critical length. Also, maximum fiber stress occurs at x $= l_c / 2$. Therefore the above equation can be written as

$$\tau = \sigma_f d / 2 l_c \tag{2.4}$$

where d is the diameter of a circular fiber. Because the fiber-matrix interface is placed under shear, the calculated value of τ should be an excellent predictor of the interfacial shear strength. Because the tensile strength is characteristic of a particular fiber type, the ratio of the critical length to fiber diameter is the important parametric combination. l_c / d is often called the critical aspect ratio.

In practice, there is a distribution of critical lengths. Any fragment with a length slightly exceeding l_c will break in two, yielding at the conclusion of the experiment, a random distribution of fragment lengths between $l_c / 2$ and l_c. A two parameter Weibull distribution is used to fit the data as shown in the following equation.

$$\tau = (\sigma_f / 2 \beta) \, \Gamma (1 - 1/\alpha) \tag{2.5}$$

where α and β are the scale and shape parameters from the Weibull distribution, Γ is the gamma function.

A significant advantage of this technique is the observation of the failure process in transmitted polarized light i.e. frictional debonding, interfacial crack growth parallel to the fiber-matrix interface and matrix crack growth perpendicular to the fiber axis and the locus of failure can be identified.

If the reinforcing fiber is replaced with a fiber having a ceramic coating, the same stresses are developed except that they must be transmitted through the ceramic into the fiber substrate. Since ceramics are usually stiff, brittle materials, fracture will take place within the coupon. For the preceramic inorganic polymer coatings studied here, both the failure mode and the interfacial shear strength can be quantified. By applying a tensile load to the adhesive, a shear stress is created which causes the oxide coating to fracture in regular lengths. The measurements of these lengths l combined with the physical properties of the coating (thickness t) allows the shear strength between the coating and the fiber to be determined through the use of the following equation

$$\tau = (2 + 4t/d)\, \tau_m - \sigma_f\, d / 2\, l \tag{2.6}$$

where subscript m refers to matrix.

The fragmentation test can be used to evaluate the changes in adhesion during processing as well as after fabrication. A limitation is that the fracture properties of the encapsulating polymer determine whether or not the test can be carried to completion and hence critical length can be achieved. If the test can be conducted, the critical length to coating thickness ratio and the failure mode can be determined by in situ microscopy.

The high magnification required to see the events at the interfacial region can not be accomplished by the conventional optical microscopy and the Scanning Electron Microscope (SEM) can not penetrate into the single fiber specimen. Ultramicrotoming of the specimen offers the possibility of examining the interphase directly under the high magnification capabilities of the Transmission Electron Microscope (TEM). Features such as fiber-coating failure, coating-matrix failure and coating-fiber adhesion can be identified by this procedure.

2.3.2 Microindentation Technique

Another approach for the characterization of the shear strength of the interphase was first proposed by Mandell and coworkers **[17,18]**. In this technique, single fibers perpendicular to a cut and polished surface of a regular high volume fraction composite are compressively loaded to produce debonding and/or fiber slippage as shown in **Figure 2.3**. In contrast to methods which use a simplified single fiber composite model system to provide information on fiber-matrix adhesion, the microindentation method is an in situ interface test conducted on actual sections of real composites and therefore has the advantage of reflecting actual processing conditions. It can allow determination of the interface strength due to fatigue or environmental exposure or possibly monitor interface properties of parts in service. If a carbon fiber with its ceramic coating is encapsulated in a polymeric matrix and subjected to the same microindentation procedures as a reinforcing fiber alone, the response of the system should be solely dependent on the interphase and its mechanical properties.

The microindentation method is conducted on a specially constructed apparatus called an interfacial testing system (ITS) as shown in the **Figure 2.3**. The measurement of the force-displacement curve which is measured during the indentation tests can identify the failure load and hence the adhesion or interfacial shear strength. Closer inspection of the force-displacement curve can also be used to quantify the properties of the interphase

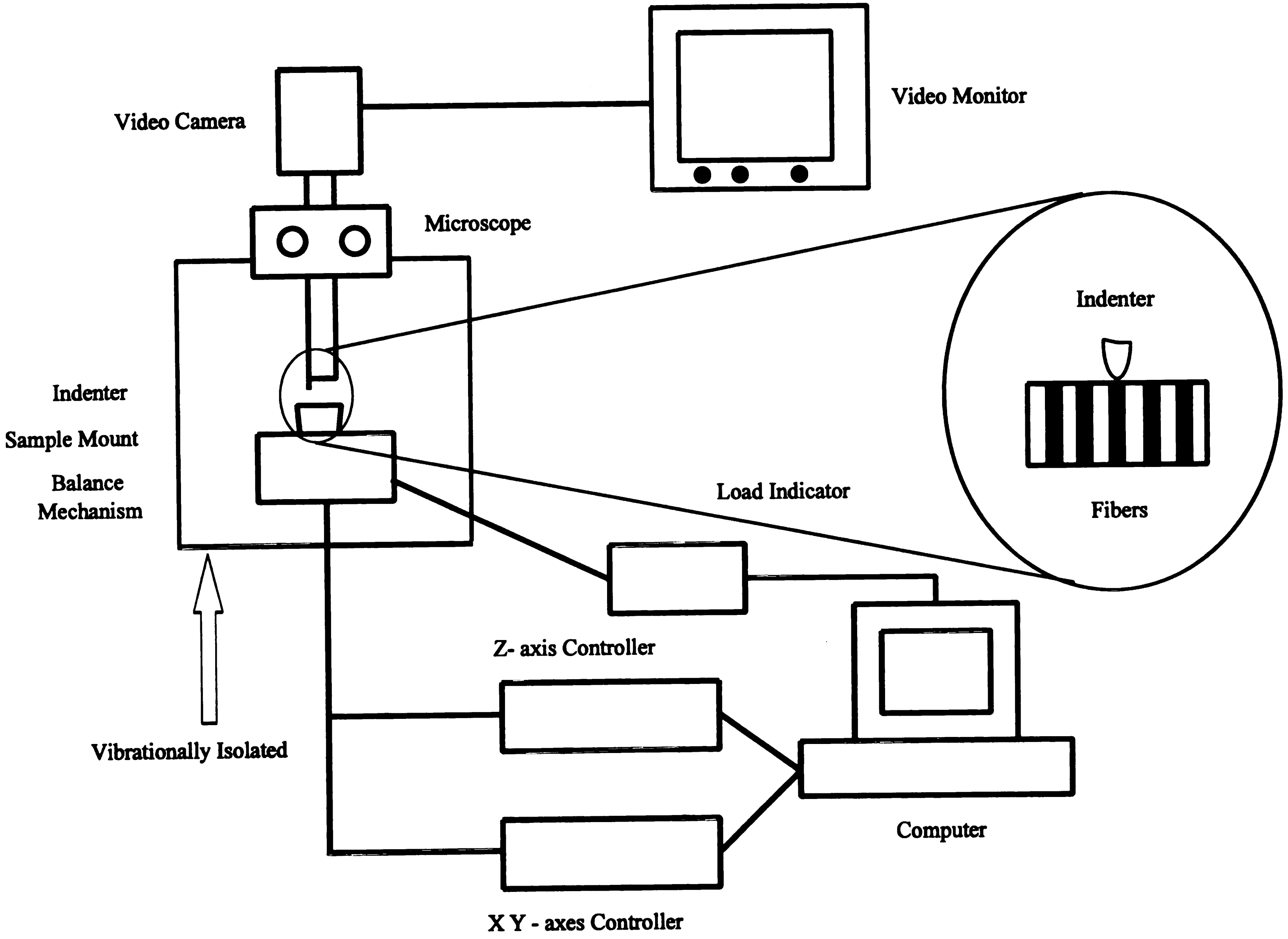

Figure 2.3 Schematic of Interfacial Testing System

as well as to delineate the failure mode. Although one data point is determined for each fiber tested, sample manipulation and automation procedures make data collection very efficient. This method is very good for making relative measurements within the same system and would also be ideal in a quality control environment.

Interfacial shear strength is calculated through the use of a finite element analysis of the stressed area for each fiber under examination. The microindentation test is done on individual selected fiber which is surrounded by neighboring fibers located at various distances and distributed in a variety of arrangements, which range from a hexagonal array to random and dispersed configurations. The diameter of the tested fiber and the distance to the nearest neighbor fiber are recorded for each test and a simplified axisymmetric finite element model (FEM) is used. This model includes the fiber, surrounding matrix, and average composite properties beyond the matrix. Maximum interfacial shear stress occurs at a distance that is a fraction of a fiber diameter below the free surface for most cases. It is assumed that debonding initiates at this point due to shear stress. The maximum shear stress along the interface is insensitive to probe stiffness as long as the contact area does not approach the interface. The maximum shear stress is significantly affected by the relative elastic constants of the fiber and matrix as well as the thickness of the matrix layer. In practice, the elastic constants are known to within a good approximation under most conditions. In the finite element model, the thickness of the matrix layer is an approximation and is intended to represent the local fiber arrangement and spacing. The actual matrix layer is always nonsymmetrical, with significantly different distances to neighboring fibers in different directions. The effect of actual local fiber arrangement can not be included in a simple data reduction scheme. The most important aspect of fiber arrangement is the distance to the nearest neighbor fiber.

Calculations of interfacial shear strength assume either a maximum interfacial shear stress criterion or a maximum radial tensile stress criterion, ignoring other stress components and residual stresses in both cases. The interfacial shear strength (τ_i) is calculated from:

$$\tau_i = \sigma_{fd} \, (\tau_{max} / \bar{\sigma}_f)_{FEM} \tag{2.7}$$

where σ_{fd} is the average compressive stress applied to the fiber end at debonding and $(\tau_{max}/\bar{\sigma}_f)_{FEM}$ is the ratio of the maximum shear stress to applied stress. Calculations of the interfacial tensile strength σ_{ri} for tensile radial stress at the surface is given by:

$$\sigma_{ri} = \sigma_{fd} \, (\sigma_{r/max} / \bar{\sigma}_f)_{FEM} \tag{2.8}$$

where $(\sigma_{r/max} / \bar{\sigma}_f)_{FEM}$ is the ratio of the maximum radial tensile stress at the surface to the applied fiber pressure resulting from the finite element analysis. In all cases, the FEM results are calculated for the ratio of matrix layer thickness to fiber diameter of 0.4.

2.4 CARBON FIBERS

Continuous filament carbon fibers are produced by pyrolyzing, or decomposing by heating, fibers that contain enough carbon so that the resultant carbon fiber is both physically and economically attractive. Carbon fibers are derived from three major feedstock or precursor sources: rayon, polyacrylonitrile, and petroleum pitch. Rayon precursors are derived from cellulosic materials and were one of the earliest precursors used to make carbon fibers. Their advantages were that they were well characterized and readily available; their most significant disadvantage was a relatively high weight loss, or low conversion yield to carbon fiber. Polyacrylonitrile (PAN) precursors are the basis for the majority of carbon fibers commercially available today.

The carbon fibers used in this study are pitch based. Pitch precursors are based on petroleum asphalt, coal tar, and polyvinyl chloride. Pitches are relatively low in cost and high in carbon yield. Their most significant drawback is nonuniformity from batch to batch. Sizings (coatings) and finishes are often applied to fiber bundles (tows) to improve their handling characteristics. They must be formulated to adhere to but not to interfere with the performance of the composite. A sizing may incidentally react chemically with the surface. The fibers are also surface treated to chemically modify the nascent fiber surface that alters the surface chemical composition, such as oxidation, acid-base reactions, and etching, without a deliberate coating of the surface. A surface treatment may incidentally result in the formation of a coating.

High strength, high modulus carbon fibers are about 7 to 12 μm in diameter and consist of small crystallites of "turbostratic" graphite, one of the allotropic forms of carbon. In a graphite single crystal the carbon atoms are arranged in hexagonal arrays which are stacked on top of each other in a regular ABAB . . . sequence. The atoms in the layer or basal planes are held together by very strong covalent bonds and there are weak van der Waal forces between the layers. This means that the basic crystal units are highly anisotropic. To obtain high modulus and strength the layer planes of the graphite have to be aligned parallel to the axis of the fiber. The pitch based carbon fibers have tensile modulus as high as 100x 10^6 psi (724 GPa), tensile strength of 325,000 psi (2.24 GPa) and have a density of 2.0 g/cc.

Carbon fibers are most widely used in polymer-, ceramic-, and metal-matrix composite materials.

2.5 POLYMER-DERIVED CERAMICS

The coating material used in this study is a preceramic polymer. The most widely recognized ceramic products produced from polymers are fibers. However, other three uses of polymer-derived ceramics include coatings for oxidation protection, matrices for ceramic fiber-reinforced composites and nonfugitive binders for ceramics prepared from powders.

Conversion of the polymer to a stable ceramic phase (that is, pyrolysis), is done by heating in a nonreactive atmosphere such as argon, helium, or nitrogen to about 1000°C or higher. Pyrolysis is accompanied by substantial shrinkage caused by weight loss and densification. Densities of preceramic polymers are typically 1.1 to 1.2 g/cc, while polymer chars show densities of 2.3 to 2.6 g/cc. Shrinkage in fiber processing is of only minor consequence, but polymer shrinkage in the preparation of coatings can be a major concern.

The major processing steps necessary to prepare the four types of polymer-derived ceramics are shown in **Figure 2.4**.

Polymer-derived coatings have been reported to be effective in protecting carbon and metal substrates against oxidation and wear. Another advantage of polymer-derived

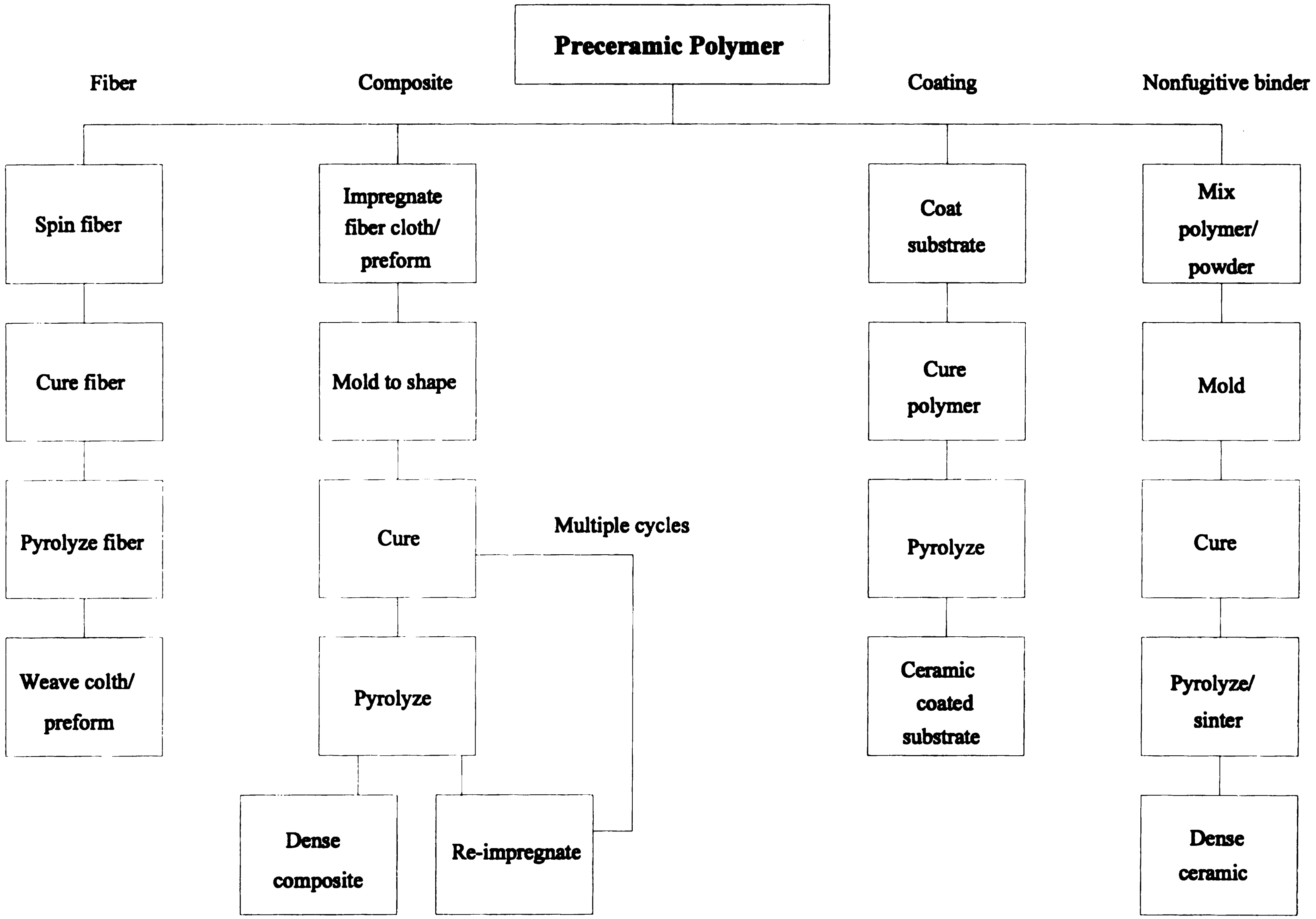

Figure 2.4 Major processing steps necessary to prepare the four types of polymer-derived ceramics.

coatings is their ease of application. The coatings can be applied by spraying, brushing or dipping.

2.6 INORGANIC PRECERAMIC POLYMER COATING

The first step in developing a detailed understanding of the fundamental factors that control interface properties and the mechanics of failure is to establish a benchmark interface and composite system, and clearly define its attendant properties. In this study, we have chosen to work with interfaces prepared using silsesquioxane terpolymer $-[MeHSiO]_{0.1}[Me(nPrO)SiO]_{0.2}[MeSi(O)_{1.5}]_{0.7}-$ because it is soluble in hexane, which is volatile and permits very facile coating of the fibers; high temperature stability in air; and because there is already considerable literature on the utility of silsesquioxanes as precursors to silicon oxycarbide, SiO_xC_y **[19-27]**. The chemical structure of this silsesquioxane terpolymer is shown in **Figure 2.5**. Moreover, $-[MeSi(O)_{1.5}]_x-$, polymethylsilsesquioxane has been used as a preceramic polymer for fabrication of silicon carbide powders**[21]**, "black glass" (70% SiO_2 /20% SiC/10% C) composite matrices for carbon fibers **[20]** and for the fabrication of black glass fibers **[28]**.

2.6.1 Synthesis

The above silsesquioxane terpolymer is synthesized via reactions (2.9) and (2.10): **[29,19]**. The copolymer is produced by catalytic redistribution of $-[MeHSiO]_x-$ oligomer using dimethyltitanocene, Cp_2TiMe_2 as the catalyst precursor.

$$-[MeHSiO]_x- \xrightarrow{Cp_2TiMe_2/\ 20^{\circ}C} MeSiH_3 + -[MeHSiO]_{0.3}[MeSi(O)_{1.5}]_{0.7}- \qquad (2.9)$$

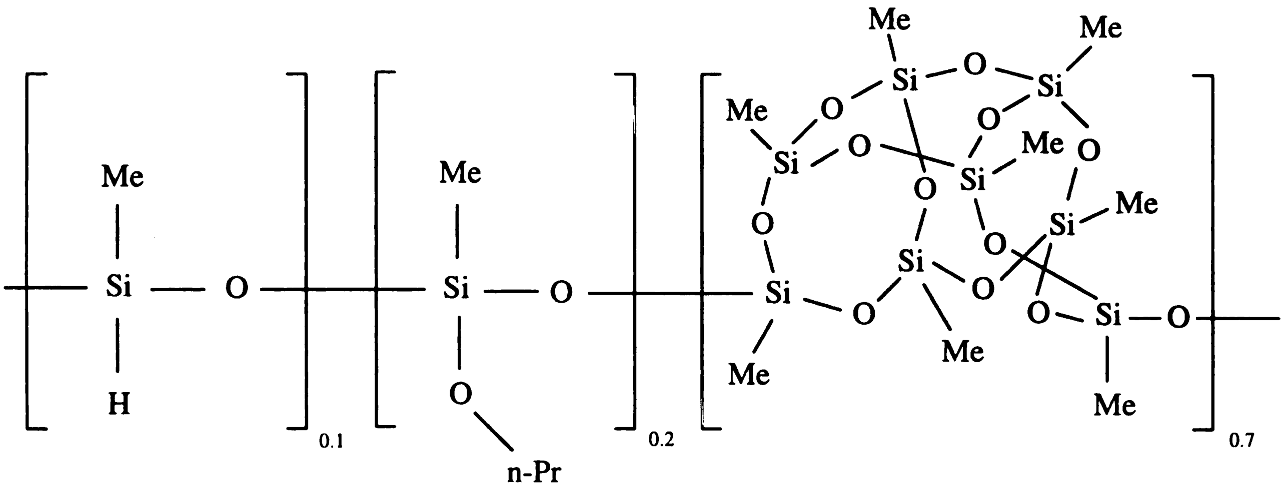

Figure 2.5 Chemical structure of silsesquioxane terpolymer

Following catalytic redistribution, the resulting copolymer, $-[MeHSiO]_{0.3}[MeSi(O)_{1.5}]_{0.7}-$ is reacted with n-propyl alcohol as follows to give the required product.

$$-[MeHSiO]_{0.3}[MeSi(O)_{1.5}]_{0.7}- + n\ PrOH \xrightarrow{Cp_2TiMe_2/\ 20^{\circ}C/-H_2} -[MeHSiO]_{0.1}[Me(nPrO)SiO]_{0.2}[MeSi(O)_{1.5}]_{0.7}- \qquad (2.10)$$

The exact ratio of monomer units was determined by proton NMR as described elsewhere [19].

2.6.2 Pyrolytic Behavior of Bulk Silsesquioxane

The pyrolytic behavior of bulk silsesquioxane provide the basis for establishing the reaction processes that occur as the n-propoxy derivative, $-[MeHSiO]_{0.1}[Me(nPrO)SiO]_{0.2}[MeSi(O)_{1.5}]_{0.7}-$, transforms to SiO_xC_y on heating.

Diffuse Reflectance Infrared Fourier Transform (DRIFTS) and solid state Magic Angle Spinning Nuclear Magnetic Resonance (MAS NMR) show that on heating to 900°C-1000°C in increments of 200 °C (one hour holds), $-[MeHSiO]_{0.3}[MeSi(O)_{1.5}]_{0.7}-$ undergoes well defined changes in structure [1]. The copolymer is stable to 200 °C; however on heating to 400 °C it loses the starting monomer units and transforms to a polymer consisting solely of $-[MeSi(O)_{1.5}]_x-$ or "T" monomer units. This clear material is relatively stable on heating for one hour at 600 °C. The MAS NMR indicates a slight redistribution of the T groups to form a material with a composition of $-[(CH_2)_2SiO]_{0.1}[SiO_2]_{0.1}[MeSi(O)_{1.5}]_{0.8}-$. At 800 °C, redistribution is more pronounced giving a product with a composition of $-[(CH_2)_2SiO]_{0.2}[SiO_2]_{0.3}[MeSi(O)_{1.5}]_{0.5}-$. In this instance, some of the Si-C bonds are cleaved and free carbon is formed. The process is much more extensive at 1000 °C. Heating silsesquioxanes to temperatures above 1300 °C results in the formation of SiO_2 and SiC **[21,22]**. A Thermogravimetric Analysis (TGA) of this terpolymer shows a ceramic yield of 86% at 1000 °C. The high ceramic yield is important because it indicates that during composite processing, the interface material will contribute minimally to offgassing. Two main features of TGA are 6-7% mass loss that occurs between 400 °C to 600 °C and the 11-12% mass loss at 600 °C to 800 °C. The first mass loss likely corresponds to elimination of -[MeHSiO]- units. The second mass loss likely to correspond to hydrocarbon materials, perhaps through fragmentation of the propoxy groups. The terpolymer does not undergo any mineralization processes up to 600 °C. The 800 °C and 1000 °C DRIFT spectra contrast greatly with the spectra seen at lower temperatures. The sharp IR absorption seen for molecular vibrations give way to the broad, featureless bands common for amorphous SiO_xC_y materials **[25,27,30]**. The mineralization occurs above 600 °C. The polymer undergoes volumetric shrinkage and becomes more dense and probably thinner as it transforms into ceramic.

2.6.3 Oxidation Resistance

The carbon fibers are not stable above about 600 °C in air. One of the purposes of the coating on carbon fibers is to prevent the fiber from rapid oxidization. The resistance to air oxidation should also be a measure of resistance to chemical damage during composite processing, e.g. during infiltration of molten metals into woven preforms. The oxidation studies carried out on P-55 carbon fiber show that 0.1 μm thick coating increase fiber oxidation resistance by 75 °C to 100 °C relative to the uncoated fiber **[1]**. This increased oxidation resistance may be sufficient to warrant efforts to make graphite fiber aluminum matrix composite materials.

2.6.4 Coating Method and Pyrolysis

The procedures for coating the carbon fibers begin with removing the carbon fiber sizing by heating tows of fibers in a sealed quartz tube to 900 °C in the presence of nitrogen for one hour in a single zone Lindberg tube furnace equipped with a Eurotherm programmable temperature controller. Tows of the fibers 60 to 80 cm in length are wrapped lengthwise on a 20×5×0.6 cm graphite rack and placed inside a ported quartz tube. The quartz tube is then sealed with a cap, inserted into the furnace, connected to a supply of dry, compressed nitrogen and then heated at 20 °C/minute to 900 °C followed by a 1 hour hold. The samples are then allowed to furnace cool. The resulting desized tows are then coated with the silsesquioxane as follows.

The rack containing the desized tows is dipped into a 2.5 wt.% solution of the silsesquioxane in hexane, allowed to stand for 1-2 minute, removed and allowed to dry for a period of 5 minutes in air. The dried fibers are again placed in the ported quartz tube and flushed and dried in a flow of nitrogen for a minimum of 10 minutes to ensure removal of any remaining solvent. The system is then heated (20 °C/minute/N_2) to selected temperatures (200 °C, 400 °C, 600 °C, 800 °C, 1000 °C) and held at temperature for 1 hour followed by furnace cooling. The pyrolyzed, coated tows are unloaded at room temperature and then stored in air prior to an analysis.

2.7 COATING CHARACTERIZATION METHODOLOGY

The characterization of the fiber coatings during thermal processing can be followed through single fiber measurements. Coating and/or interfacial coating/fiber failure due to mismatches in coefficient of thermal expansion, residual processing stresses, etc. can be identified at the nano- or microstructural level. Both adhesion strengths and failure modes can be quantified using embedded single fiber methods developed for polymers as well as using microindentation methods (ITS) to test the in-situ fiber-matrix interface on real fiber-coating-matrix systems of interest if the effect of the polymer matrix is taken into account. A complicating factor is the expected large change of fiber coating mechanical properties associated with the conversion from inorganic polymer coating to ceramic. By the selective use of single fiber specimens in transparent organic and inorganic matrices, stress states can be induced that duplicate those encountered in real composites during and after high temperature processing. A 3 dimensional model of a single fiber in the matrix can be used to quantify the stress states and optimize the processing steps.

The methodology can be coupled with the application of fiber coatings of known composition and thickness as an evaluation and optimization tool for their development. It is expected that determination of this information will lead to a protocol for optimization of the processing, as well as the properties of the fiber coatings.

CHAPTER 3

EXPERIMENTAL

3.1 MATERIALS

The carbon fibers used in this study are AMOCO's Thornel™ P-55. Some properties of the fiber are given in **Table 3.1(a)**. The fibers were coated with the preceramic silsesquioxane polymer and were pyrolyzed. Tows of the Thornel P-55 graphite fibers, 60-80 cm in length, were wrapped lengthwise on a 20 cm × 5 cm × 0.6 cm graphite rack and placed inside a ported quartz tube. (1) The quartz tube was then sealed with a cap, inserted into the furnace, connected to a supply of dry, compressed nitrogen and then heated at 20 °C/minute to 900 °C followed by a 1 hour hold. The samples were then allowed to furnace cool. (2) The resulting desized tows were dipped into a 2.5 wt.% solution of the silsesquioxane in hexane, allowed to stand for 1-2 minutes, removed and allowed to dry for a period of 5 minutes in air. (3) The dried fibers were again placed in the ported quartz tube and flushed (and dried) in a flow of nitrogen for a minimum of 10 minutes to ensure removal of any remaining solvents. (4) The system was then heated (20 °C/minute in nitrogen) to selected temperatures (200 °C, 400 °C, 600 °C, 800 °C and 1000 °C) and held at temperature for 1 hour followed by furnace cooling. The pyrolyzed tows were carefully handled at room temperature to prevent damage to the coating by inadvertent flexing of the fibers.

(a) Thornel P-55 carbon fiber

Diameter	10 μm to 13 μm
Tensile Strength	1.9 GPa
Tensile Modulus	380 GPa
Density	2.0 g/ml

(b) Epon 828 Epoxy

Tensile Modulus	3.6 GPa
Tensile Strength	89.6 MPa
Shear Modulus	1.24 GPa

Table 3.1 Properties of (a) Thornel P-55 carbon fibers and (b) EPON 828 epoxy matrix cured with 14.5 wt.% of mPDA.

The polymer matrix used in this study is the EPON® 828 epoxy resin (Shell Chemical Company, Houston, Texas) cured with *meta*-phenylene diamine (mPDA) (Aldrich Chemical Company). The 828 epoxy resin is an undiluted diglycidyl ether of Bisphenol A. mPDA is in flake form. The chemical structures of the epoxy and the curing agent are shown in **Figure 3.1**. The epoxy was mixed with 14.5 wt.% mPDA, degassed under vacuum for 2-5 minutes and air-cured for two hours at 75 °C and two hours at 125 °C in an oven. The resulting matrix has the properties given in **Table 3.1(b)**.

3.2 ADHESION CHARACTERIZATION

The adhesion characterization was done by (i) The Single Fiber Fragmentation Test and (ii) The Microindentation or the ITS (Interfacial Testing System) test. Experimental procedures for these tests are given below.

3.2.1 Single Fiber Fragmentation Test

A description of this method is given in section 2.3.1. The fabrication of the dog-bone specimen and alignment of the fiber was accomplished by the aid of silicon RTV-664 [31] eight cavity mold of 1 inch long gage length, about 1/8 inch wide and 1/16 inch deep as shown in **Figure 3.2 (a)**. Single fibers of approximately six inches in length were selected from the fiber bundle by hand. The fibers were separated with a flowing air stream and handled only at ends. Once selected, a fiber was mounted in the mold cavity and held in place with a small amount of rubber cement at the ends of the sprue of the mold. The rubber cement does not come in contact with the cavity which contains the gage length section of the fiber.

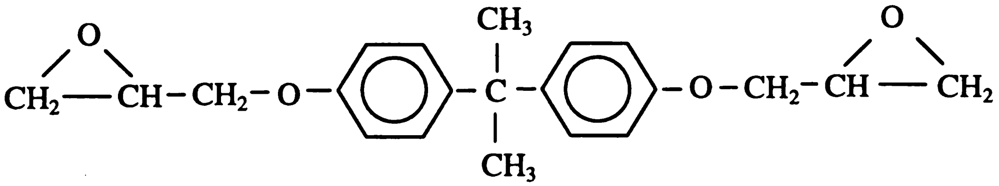

(a) Diglycidyl Ether of Bisphenol-A

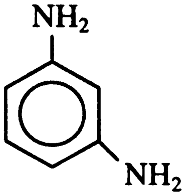

(b) *meta* -Phenylene diamine

Figure 3.1 Chemical structures of (a) EPON 828 epoxy and (b) curing agent.

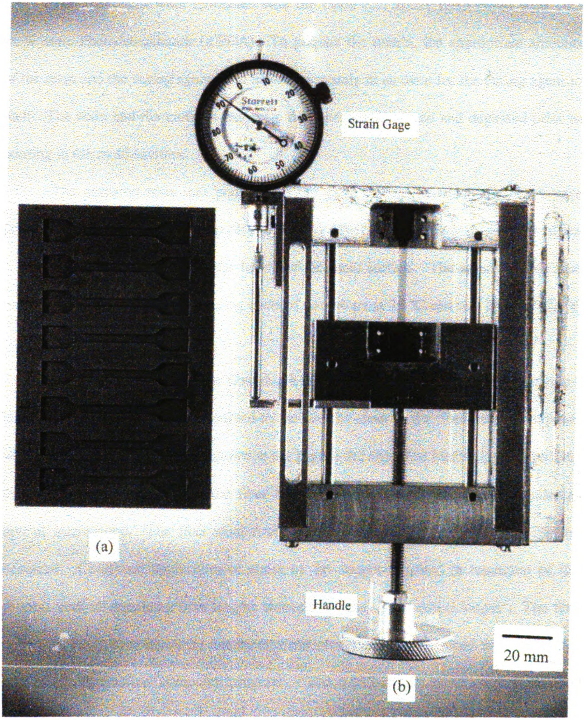

Figure 3.2 (a) Silicon mold and (b) Loading jig used in the Single Fiber Fragmentation Test.

The specimens were fabricated with the Epon 828 epoxy resin cured with 14.5 wt.% *meta*-Phenylenediamine (mPDA). To prepare the matrix, the appropriate amounts of the resin and the curing agent were heated separately in an oven for the curing agent to melt. The resin and the curing agent were then thoroughly mixed and degassed prior to pouring in the mold cavities.

The prepared resin was poured into the mold cavities in which the fibers were previously mounted with the help of a pipette to direct the resin flow to all parts of the cavity and to a level just above the height of the mold surface. The assembly was then transferred to an oven where a curing cycle of two hours at 75 °C and two hour at 125 °C was completed.

Once fabricated, the single fiber dog-bone coupons were then tested by applying a tensile load axially which is transmitted to the fiber by shear at the fiber-matrix interphase with the help of a loading jig as shown in the **Figure 3.2 (b)**. The loading jig can be fixed on an optical microscope and the fiber fracturing phenomena was observed under an optical microscope. The fiber axial stress rises from the ends until the fiber fracture occurred. Continued application of stress to the coupon resulted in repetition of this process until all remaining fiber lengths were shorter than the "critical length". The fiber critical length (l_c) and hence the interfacial shear strength were determined with the help of a Weibull distribution computer program. The interfacial shear strength is a good estimator of the adhesion between fiber and matrix. The transparent nature of the matrix allows to see transmitted polarized light photoelastic stress patterns in the dog-bone coupon under stress and different failure modes can also be seen, as photo-elasticity is the science which deals with the effects of stress upon light traversing transparent materials. This can be accomplished by placing the specimen between two sheets of polarizing material that have been oriented so that their axes of polarization are perpendicular and viewing the specimen against a source of even diffuse light, such as a light table. A coupon with no defects will show a relatively smooth graduation of intensity from the edges to the center of the gage section. This pattern represents stresses induced by the different coefficients of thermal expansion of the matrix, the silicon mold and the graphite fiber during the cure cycle of the resin. Specimens with defects in or near the fiber will show distinct stress patterns at these points. These stress patterns need the help of an optical microscope in order to be seen. Even though the coupon is transparent, the surfaces of the coupon are seldom optically flat. A fluid of the same index of refraction as the 828 matrix when introduced between the coupon and a cover glass placed on the coupon greatly reduces image blurring due to the irregular surfaces of the coupon and insures repeatable magnification of the coupon. The cover glass can be used on the top surface as well as on the bottom surface of the coupon. The surface tension of the fluid is sufficient to hold the lower cover glass in place.

3.2.2 Microindentation or Inerfacial Testing System (ITS) Test

A description of this test is given in the section 2.3.2. The ITS test is conducted on the stage of an optical microscope. A diamond-tipped probe, which is mounted on the objective lens holder of the microscope, is used to push single fibers from their surrounding matrix. Initiation of fiber debonding results in a load drop that is sensed by a load cell attached to the specimen holder. The parameter of interest in this test is interfacial shear strength which is a derived rather than a directly measured value. To prepare a specimen for testing, many fibers were embedded in the Epon 828 epoxy matrix and then cut into small pieces which were then embedded in a metallographic specimen mount with the fibers normal to the specimen surface. This specimen is a ring of about 1 inch in diameter and 3/4 inch in height. Grinding and polishing the surface were done using conventional metallographic techniques. A good specimen should be free from any debonding of the fibers. The specimen was placed on the microscope stage and the operator begins the test by specifying the testing variables from a series of menus on the computer screen. The operator then selects a good fiber to be tested by moving the motorized stage with linear motion in all three axes (**Figure 2.3**). The most important aspect of fiber arrangement is the distance to the nearest neighbor fiber. The test is begun by moving the fiber to be tested directly beneath the diamond-tipped indenter. A 10 μm diameter diamond indenter was used. The stage then rises at a pre-selected rate until the indenter contacts the fiber. In automatic operation, the stage continues to rise until debond is attained, as measured by the pre-selected load drop criterion. In semi-automatic operation, the operator can interact at any stage of the test by stopping the continuation of load and can look at the degree of debond. A graph of load versus stage displacement is shown on the computer monitor as the test runs. The operator can change the debond criterion. The semi-automatic operation and 120° debond criteria were used to determine the interfacial shear strength in all the tests.

3.3 COATING UNIFORMITY and THICKNESS

Scanning Electron Microscope (SEM) and Environmental Scanning Electron Microscope (ESEM) were used to observe the surface uniformity / topography of the fibers. The surface analytical technique of Auger Electron Spectroscopy (AES) was used to determine the thickness of the fiber coatings and how they changed with processing.

Topography of the fiber surface was characterized by a JEOL JSM-T330 SEM (Scanning Electron Microscope) and by an ElectroScan ESEM (Evironmental Scanning Electron Microscope) model 2020.

The ESEM has the advantage of examining specimens in gas/water vapor upto 50 torr at temperatures of -160 °C to +1000 °C and positive ions formed in the process neutralize the negative surface charge that can build up on an insulating specimen, and coatings to prevent charging are not required.

The AES technique is based on the similar process as the XPS technique, except that in AES the surface is irradiated with a beam of electrons. The incident electrons ionize atoms of the surface creating vacancies in their inner electron shell. When an electron is ejected from an inner shell of an atom the resultant vacancy is soon filled by an electron from one of the outer shells (**Figure 3.3**). The energy released may appear either as an X-ray photon, the characteristic X-rays used in electron probe microanalysis and in X-ray fluorescence spectroscopy, or be transferred to another electron which is ejected from the atom (Auger electron) with an energy, E_A, determined by the three energy levels concerned, where

$$E_A = E_1 - E_2 - E_3 \qquad (3.1)$$

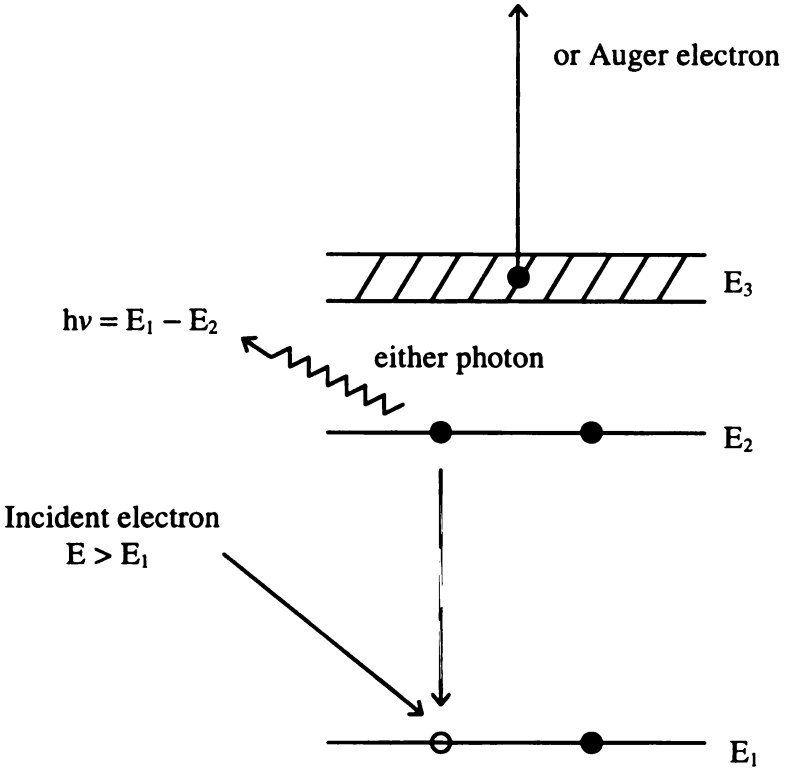

Figure 3.3 Characteristic X-ray and Auger electron production.

E_1 and E_2 are the binding energies of the atom in the singly ionized state while E_3 is that of the doubly ionized state. The Auger electrons are detected by an electron spectrometer. Auger transitions are typically denoted by three capital letters such as KLL, LMM, MNN etc. The letter on the left refers to the electron shell in which the initial vacancy occurred; the middle letter refers to the shell from which an electron comes to fill the initial vacancy; and the letter on the right refers to the shell from which Auger electron is emitted. For lower energy events leading to a photon or electron with energy less than 2 keV the Auger process is dominant with more than 95% of ionizations leading to the ejection of Auger electron. A primary electron beam of energy between 5 and 10 keV is employed to achieve the Auger effect.

The AES technique, similar to the XPS technique, only examines the electrons that originate within the tens of angstroms of the top surface region. The principle advantage of the AES over XPS technique is the ability to focus and scan the probing electron beam, and obtain information on the spatial distribution of surface elements at high magnifications. AES has the capability to map elements and it is less sensitive to the chemical environment of the elements than the XPS technique.

The AES technique is well suited to composition-depth profiling and hence for the analysis of thin films and surface coatings. The bombardment of a target surface is accomplished with inert argon ions. A surface atom or molecule becomes sputtered if the energy transferred to it is greater than its surface binding energy and the imparted momentum has a component normal to the surface.

The coated fibers were mounted on a stage horizontally and clamped from both ends and then analyzed by AES for the determination of coating thickness by determining the composition profile as the ion beam sputtered through the coating. Individual fibers were selected for the sputtering at magnifications between 5000X-7000X and 2 × 2 mm raster area was used for all the fibers. The sputter rate calibration of the ion gun was determined (for SiO_2) to be 106 °A / minute. 10 kV electron beam energy was used. All the AES analyses were carried out using Perkin-Elmer Physical Electronics (PHI) model 660 Scanning Auger Multiprobe.

3.4 COATING CHEMISTRY and COMPOSITION CHARACTERIZATION

X-ray Photoelectron Spectroscopy (XPS) surface analysis was used to determine the compositional change in the 0.1 μm thick coatings as they were being thermally processed from 200 °C to 1000 °C with increments of 200 °C. XPS is also known as Electron Spectroscopy for Chemical Analysis (ESCA), though the title XPS is more scientifically correct than ESCA.

In XPS, the sample is illuminated with X-rays under ultra-high vacuum conditions which excite photoelectrons from the surface **[32]**. Mg Kα X-rays (1253.6 eV) or Al Kα X-rays (1486.6eV) are commonly used. The resultant photoelectrons have a kinetic energy (E_k) which is related to the X-ray energy ($h\nu$) and the binding energy (E_b) of each core electron (which is characteristic of the individual atom to which it is bound) by the Einstein relation **[33]**:

$$E_k = h\nu - E_b \tag{3.2}$$

The photoemission is observed by measuring the energy spectrum of the emitted photoelectrons by an electron spectrometer. The photoelectron energy is dependent on the precise chemical configuration of the surface atoms. The emitted photoelectrons can escape from tens of angtroms of the solid surface.

The silsesquioxane coated carbon fibers heat treated at 200 °C, 400 °C, 600 °C, 800 °C and 1000 °C temperatures were mounted on a stage horizontally and clamped from both ends and then analyzed by XPS to see the change in composition of the coating as a function of heat treatment temperature. Although the mean free path of the photoelectrons was only 1-2 nm, the composition measures were taken as an indication of the bulk composition of the coating. XPS analyses were conducted on a Perkin-Elmer PHI 5400 ESCA system using an Al Kα source. Spectra were collected at a base pressure of approximately 10^{-9} torr and electron take-off angle of 65° using a position sensitive detector (PSD) on a 180° hemispherical analyzer set at 89.45 eV pass energy for the survey scans (0-1200 eV) and 35.75 eV for the narrow scans of the elemental regions used for composition analysis.

3.5 ULTRAMICROTOMY and TRANSMISSION ELECTRON MICROSCOPY

To identify the nature of the interfacial region and the locus of interfacial failure (i.e. coating-fiber or coating-matrix) we need to look at the region of interest in the single fiber dog-bone coupon. The high magnification required to see the events at the interfacial region can not be accomplished by the conventional optical microscopy and the SEM can not penetrate into the single fiber specimen. Ultramicrotoming of the specimen offers the possibility of examining / analyzing the interphase directly under the high magnification capabilities of the Transmission Electron Microscope (TEM) along with the energy dispersive X-ray analysis.

The TEM samples must be thin enough to transmit sufficient electrons to form an image. The samples must also be stable under the electron beam and in a high vacuum. The TEM is designed to provide the information from the interactions of electrons (elastic, inelastic) as they pass through the specimen. This is most commonly manifested as a two dimensional projection of those events transduced to a light signal viewed on a fluorescent screen. Increasing the sample thickness increases the beam absorption and reduces the image resolution and sample stability. The practical sample thickness is limited to 100 nm for a 100 kV electron beam.

Malis *et al.* [34] have reviewed the ultramicrotoming techniques for materials science which cover metallic and ceramic materials. Following is a procedure for ultra-thin microtomy of fiber-epoxy matrix interface of the single fiber specimen.

Small pieces (~ 2-4 mm) were cut from the dog-bone specimen and were embedded in a polymer matrix in order to facilitate grip of the sample in the sample holder. A rectangular block of 5 × 10 mm is typical. The block is then hand trimmed into a trapezoid of dimensions no longer than 0.25 mm. A thin layer of the epoxy matrix is there over the fiber. This layer was then further cut by using a glass knife to make it smooth and to avoid unnecessary use of the diamond knife which is required for the ultra-thin microtoming. A 55° (mounting angle) diamond knife was used. The knife was mounted at 4° (to the vertical axis) in the knife holder towards the block. The knife was set at a cutting angle of 15-20° to the fiber as shown in **Figure 3.4 (a)** in order to get an artifact free elliptical shaped fiber in the matrix (**Figure 3.4 (b)**). A solution of de-ionized water with low concentration of acetone (i.e. ~ 1 drop of acetone per 20 ml of the water) was used to fill the diamond knife boat with the help of a syringe. Acetone reduces the contact angle of the water to produce better wetting of the knife edge. Initially, the boat was filled to the brink of overflow and then excess water was drawn off to form a concave fluid surface behind the diamond knife. This procedure ensures good wetting of the knife edge. The knife was advanced manually towards the block face until reflection of the block face off the water meniscus was observed. The knife was then slowly advanced towards the block at 1 μm steps until cutting begins. Several 1 μm sections were cut to remove the trimming artifacts and prepare a clean smooth face for the ultra-thin sectioning. Motorized sample advancing was turned on and a cutting speed of 0.3 mm/sec was selected. The longer side of the trapezoid was set to be the lower side which first comes in contact with the knife. This procedure helps identify the cutting direction of the knife. The thickness of the sections was set at 60-100 nm to obtain silver-gold colored sections.

The sections remain attached and form ribbons (**Figure 3.4 (b)**) that float on the water. To manipulate the ribbons, an eyelash applicator was prepared. An eyelash applicator is simply an eyelash mounted on a small round wooden stick using a drop of white correction fluid or nail polish. The ribbons were assembled with the help of the eyelash applicator for the pick up by a TEM grid.

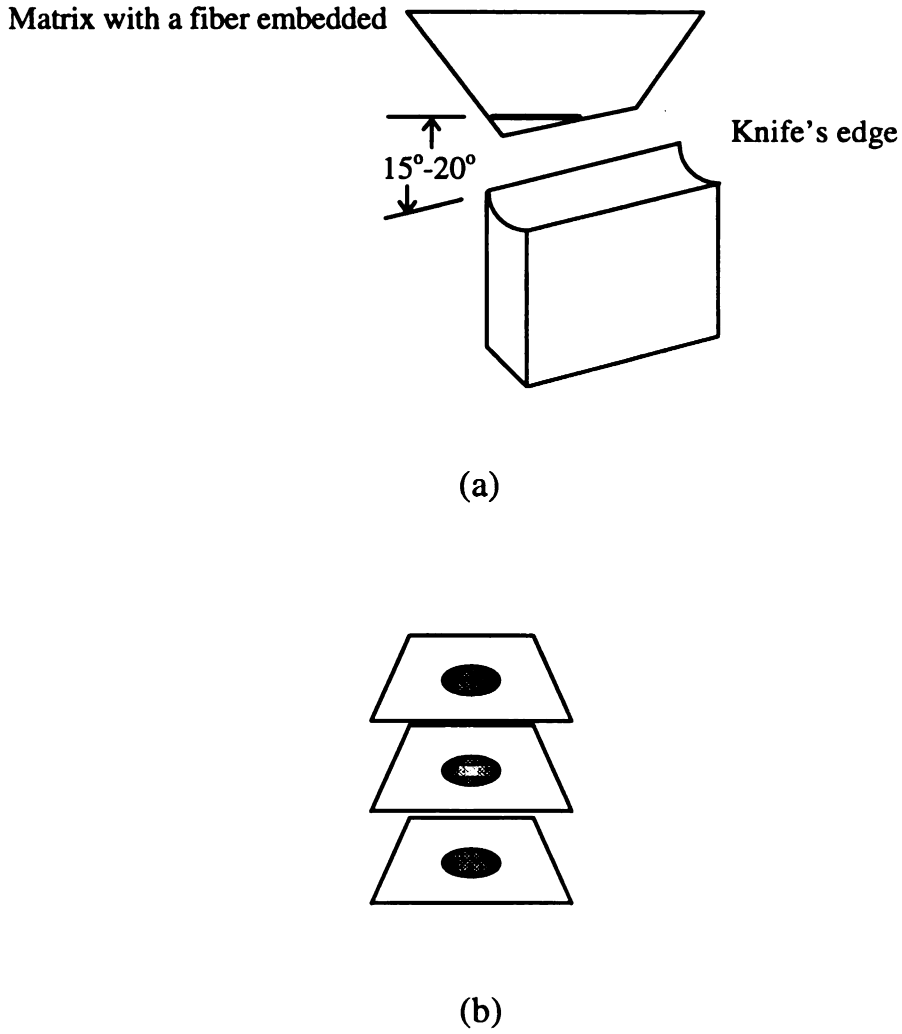

Figure 3.4 Schematic representation of (a) a top view showing the cutting angle to the fiber and (b) a ribbon formed by the sections (in which the fiber is in an elliptical shape) in ultramicrotomy (diagram is not to scale).

To collect the sections, the knife is receded and the ribbons are arranged away from the knife edge with the help of the eyelash applicator. The TEM grids used were 200 or 300 mesh formvar coated copper grids stabilized with carbon. A grid is picked up by a tweezer and under the microscope of the microtome it is placed lightly over the top of ribbons and is then removed from the boat. The sections remain attached to the grid. The grid is then drained on a filter paper and stored for the examination under TEM.

An RMC MT-7 Ultramicrotome was used to carry out the ultramicrotoming process.

The sections were examined under a JEOL-100CX TEM at an accelerating voltage of 100 kV. The energy dispersive X-ray analyzer attached to the TEM was used to identify the material adhering to the side of the matrix in the sections.

CHAPTER 4

RESULTS

4.1 COATING UNIFORMITY and THICKNESS

Surfaces of the fibers were examined with the Scanning Electron Microscope (SEM) and Environmental Scanning Electron Microscope (ESEM). Auger sputter experiments were used to determine the thickness of the fiber coatings and how they changed with processing. **Figures** 4.1, 4.2, 4.3, 4.4, 4.5 and 4.6 show the SEM micrograph of uncoated P-55 carbon fiber, SEM micrograph of the fiber coated and heat treated at 200 °C, ESEM micrograph of the fiber coated and heat treated at 400 °C, ESEM micrograph of the fiber coated and heat treated at 600 °C, SEM micrograph of the fiber coated and heat treated at 800 °C and SEM micrograph of the fiber coated and heat treated at 1000 °C respectively. **Figure 4.1** shows the extrusion marks (striations) running along the length of the fiber and "dirt" from the manufacturing process in the uncoated Thornel™ P-55 carbon fiber. The fiber diameter range was observed to be from 10 μm to 13 μm. **Figures** 4.2 to 4.6 show the same extrusion marks and "dirt" which were the features of the uncoated fiber with the coating present on the fibers. These figures show that the coatings are continuous and reasonably thin.

The Auger sputtering results of the coated fibers are illustrated in **Figure 4.7**. Peak-to-Peak intensity is plotted against sputter time. The coating contents (i.e. oxygen

Figure 4.1 Scanning electron micrograph of the surface of uncoated P-55 carbon fibers showing axial striations and some dirt from the manufacturing process.

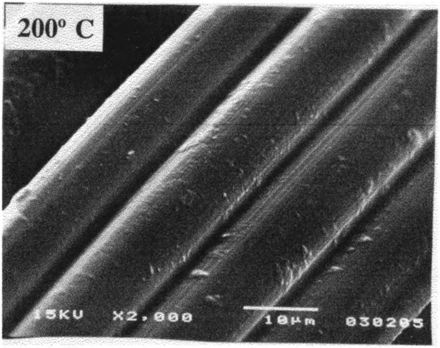

Figure 4.2 Scanning electron micrograph of 200 °C heat treated coated carbon fibers showing the same axial striations and dirt as was the case with the uncoated fibers. So, the coating is uniform.

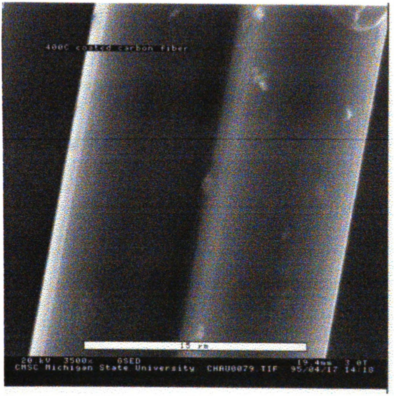

Figure 4.3 Environmental scanning electron micrograph of 400 °C heat treated coated carbon fiber.

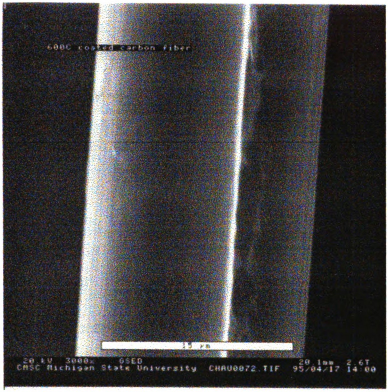

Figure 4.4 Environmental scanning electron micrograph of 600 °C heat treated coated carbon fiber.

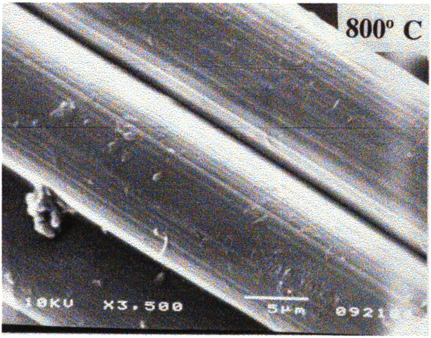

Figure 4.5 Scanning electron micrograph of 800 °C heat treated coated carbon fiber.

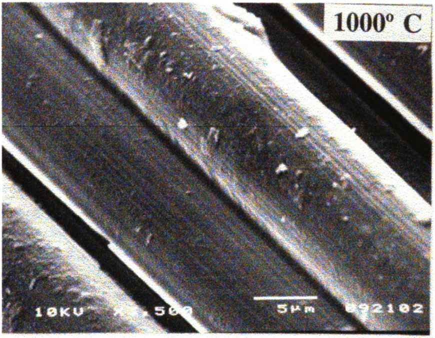

Figure 4.6 Scanning electron micrograph of 1000 °C heat treated coated carbon fibers.

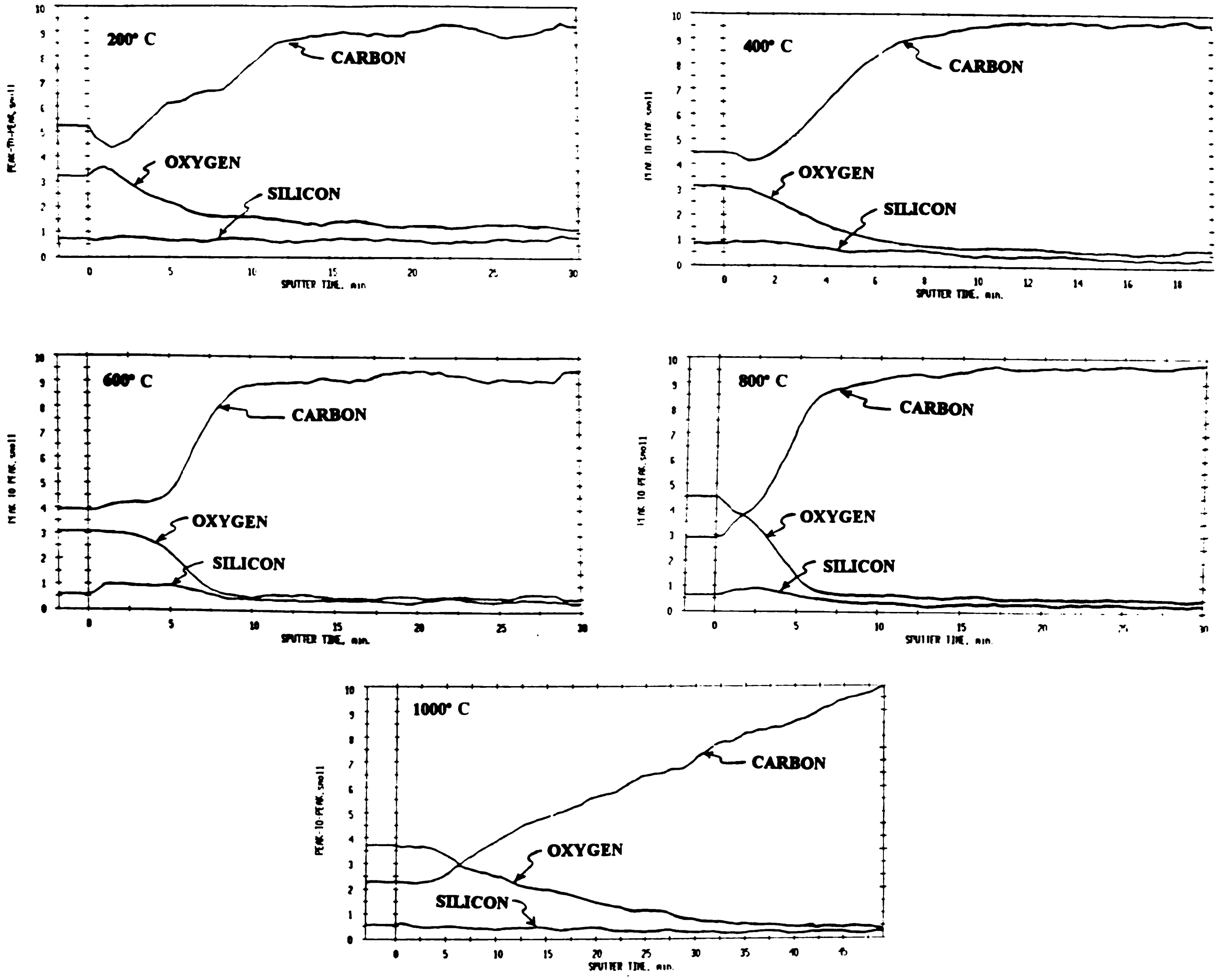

Sputter Rate = 106 °A/min

Figure 4.7 Auger sputtering profiles of silsesquioxane coated fibers pretreated to 200 °C,400 °C, 600 °C, 800 °C and 1000 °C.

and silicon) are seen to decrease with the sputter time until they reach a constant level. The silicon content of the coated fibers, however, does not decrease much with the sputter time as compared with the oxygen content. The carbon content increases with the sputter time. The sputter time for the coating contents to reach a constant level in the coated fibers treated at 200 °C, 400 °C, 600 °C and 800 °C is about 10 minutes with a calibrated sputter rate of 10.6 nm/minute. Hence the coating thickness can then be determined by multiplying the sputter time with the sputter rate. The coating thickness determined from this analysis is approximately 0.1 μm.

After 800 °C thermal treatment, the sputtering profile changes significantly for the 1000 °C case. The length of time necessary to sputter through the coating to the underlying fiber increases significantly. This can not be interpreted as due to a thicker coating. The conversion from the preceramic inorganic polymer has been completed in the 600 °C-800 °C range and the sputtering rate for the ceramic would be expected to be much lower than for the polymer. Indeed, with the weight loss of almost 14%, it would also be expected that the coating would be somewhat thinner and significantly more dense than its initial value.

4.2 COATING CHEMISTRY and COMPOSITION

X-ray Photoelectron Spectroscopy (XPS) was used to quantify the silicon, carbon and oxygen contents of the surface coatings as a function of processing temperature. **Table 4.1** shows the surface elemental composition of carbon, oxygen and silicon for the coated fibers heat treated at 200 °C, 400 °C, 600 °C, 800 °C and 1000 °C. **Table 4.2**

Table 4.1 Surface elemental composition (atomic%) of the coated carbon fiber as a function of processing temperature by X-ray Photoelectron Spectroscopy.

Element	*200 °C*	*400 °C*	*600 °C*	*800 °C*	*1000 °C*
Carbon	44	42	41	30	27
Oxygen	35	37	40	50	49
Silicon	22	20	19	21	24

Table 4.2 Ratios of surface elements by X-ray Photoelectron Spectroscopy.

Ratio	*200 °C*	*400 °C*	*600 °C*	*800 °C*	*1000 °C*
O:C	0.80	0.89	0.97	1.67	1.82
O:Si	1.62	1.83	2.13	2.38	2.04
Si:C	0.49	0.49	0.45	0.70	0.89

shows the ratios of surface elements of the coated fibers processed at 200 °C, 400 °C, 600 °C, 800 °C and 1000 °C. As seen in Table 4.1 and Table 4.2, the relative amount of silicon remains constant between 19 at.% and 24 at.% over the entire range of processing temperatures, whereas the carbon content declines from about 44 at.% to 27 at.% with a coincident increase in oxygen content from 35 at.% to 49 at.%. The trends are more clearly seen by comparing the ratios of the elements in Table 4.2. O:C, O:Si and Si:C ratios are constant through 400 °C and start to change slightly at 600 °C. Since XPS is a surface technique and the pyrolytic conversion is rate dependent to some degree, the change at 600 °C may result from the surface sensitivity of the data. The 1000 °C values of 24 at.% silicon, 49 at.% oxygen and 27 at.% carbon produce an O:Si ratio of about 2 which can be interpreted to suggest that SiO_2 and free carbon are formed, rather than SiO_xC_y.

Both the 600 °C and the 1000 °C pyrolyzed fibers appear to offer significantly improved oxidation resistance over the uncoated fibers [1]. Tows of both fibers survive 3 hours heating in air to 800 °C. Qualitatively, it was concluded that the 600 °C processed fibers survive better than the 1000 °C processed fiber coating based on the degree of surface irregularity resulting from air oxidation.

The 600 °C processed material consists of a coating of intact silsesquioxane, consisting primarily of $-[MeSi(O)_{1.5}]-$ units with all the reactive monomer units, -[MeHSiO]-, eliminated. In addition, the -[MeSi(OnPr)O]- component is likely to have decomposed to propene and new $-[MeSi(O)_{1.5}]-$ units. The resulting material is quite uniform and exhibits the well-organized high temperature stability of polymethyl silsesquioxane. In contrast, the 1000 °C material has mineralized and consists of the oxycarbide mixed with SiO_2 and free carbon. The free carbon is present as amorphous or graphitic 10-100 nm sized particles. If the amounts of free carbon are significant (10-15 wt.%), as expected, then one can view the 1000 °C material as containing the equivalent of open pores, as the free carbon will oxidize rapidly under the reaction conditions. The only reason one would not expect immediate oxidation of the fiber is because oxidation and gas transport through the resulting 10-100 nm sized pores are likely to be mass transport limited. Furthermore, some but not all the porosity generated can be expected to be interconnected, thus limiting the points at which the resulting pores penetrate to the graphite fiber below.

It can be said that it is possible to make uniform, adherent $-[MeHSiO]_{0.1}[MeSi(OnPr)O]_{0.2}[MeSi(O)_{1.5}]_{0.7}-$ silsesquioxane coatings on graphite fibers [1]. These coatings evolve chemically, on pyrolysis, to produce 0.1 μm thick coatings which increase fiber oxidation resistance by 75 °C-100 °C relative to uncoated fibers. The important questions to be answered are what are the properties of the coating and how does it adhere to the fiber surface under processing conditions encountered during metal matrix composites and ceramic matrix composites fabrication as well as under the mechanical loads expected during application.

4.3 ADHESION and FAILURE MODES

Adhesion measurements were made using the Single Fiber Fragmentation Test (SFFT) and the Microindentation test or the ITS (Interfacial Testing System) test.

4.3.1 Single Fiber Fragmentation Test

The SFFT results for the uncoated and the coated fiber treated at 200 °C, 400 °C, 600 °C, 800 °C and 1000 °C are shown in **Table 4.3** and a graphical representation of these results is given in **Figure 4.8**. The interfacial shear strength (IFSS) can be computed from the relationship given in equation (Eq.) (2.5) for the uncoated fiber and either Eq. (2.5) or Eq. (2.6) for the coated fiber depending on whether the coating acts as an integral part of the fiber (Eq. (2.5)) or as a separate layer independently of the fiber (Eq. (2.6)). The measurable parameter in either case is the fiber fragment length-to-diameter ratio (l_c/d). Eq. 2.5 was used to calculate the interfacial shear strength of the coated fibers.

Table 4.3 shows that in the Single Fiber Fragmentation Test, the uncoated fiber gives a value of the critical length-to-diameter ratio (l_c/d) of around 59. A transmitted polarized light micrograph of a typical P-55 carbon fiber under load in this single-fiber coupon is shown in **Figure 4.9**. The epoxy matrix used to fabricate the coupons is photoelastically active. The light areas are regions of high interfacial stress. The pattern displayed is typical for a system with moderate adhesion and an interfacial failure mode. An interfacial shear strength for this fiber is about 22.21 MPa.

Once the fiber is coated with the 0.1 μm silsesquioxane coating which has been heat treated at 200 °C, the critical aspect ratio (l_c/d) increases, indicating that the coating has reduced the stress transfer efficiency between the coating and the matrix. A value of interfacial shear strength of 9.33 MPa is calculated for this coated fiber. A transmitted polarized micrograph of a typical P-55 carbon fiber having the 200 °C treated coating under load is shown in **Figure 4.10**. The stress pattern is very weak, reflecting the lower

Table 4.3 Critical aspect ratio and interfacial shear strength (IFSS) determined by the single fiber fragmentation test.

Fiber Treatment	l_c / d	IFSS (MPa)
Uncoated	59 ± 9	22.21 ± 4.25
200 °C	130 ± 7	9.33 ± 0.50
400 °C	118 ± 15	10.80 ± 1.80
600 °C	107 ± 10	11.02 ± 1.32
800 °C	53 ± 4	22.60 ± 1.87
1000 °C	59 ± 6	21.28 ± 1.53

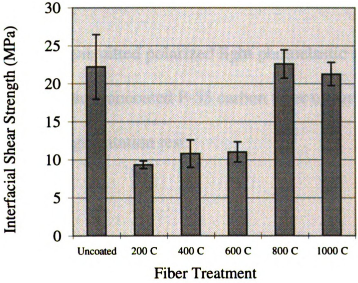

Figure 4.8 Interfacial Shear Strength Determined by the Single Fiber Fragmentation Test.

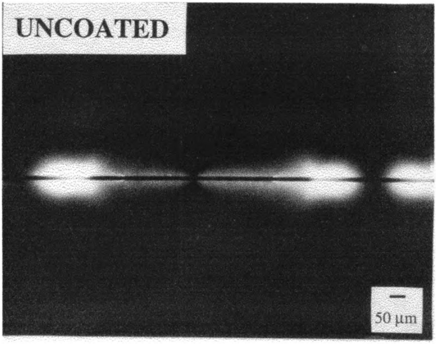

Figure 4.9 Transmitted polarized light photoelastic stress pattern of a typical uncoated P-55 carbon fiber under load in the single fiber fragmentation test.

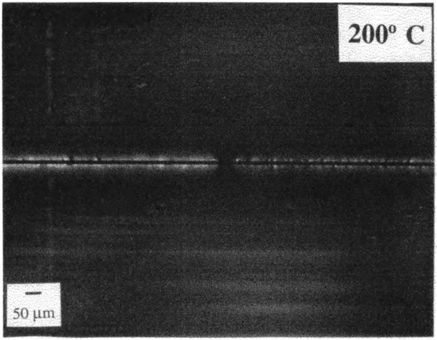

Figure 4.10 Transmitted polarized light photoelastic stress pattern of a typical 200 °C treated coated carbon fiber under load in the single fiber fragmentation test.

stresses generated at the interface. Failure appears to be interfacial between the coating and the epoxy matrix. The loss in interfacial shear strength is probably due to the low modulus of the preceramic inorganic coating. The finite element analysis discussed later concludes that adhesion as measured by the interfacial shear strength depends directly on the modulus of the coating.

Pyrolysis of the fiber coatings to 400 °C and 600 °C produces a slight upward trend in the adhesion as measured by this test. However, the error associated with the measurement is larger than the average change from 200 °C to 600 °C, making conclusions difficult. It would be reasonable to expect that the higher thermal treatments produce a more cross-linked material having a higher modulus and hence the interfacial shear strength would increase. The photoelastic stress patterns of the 400 °C and the 600 °C treated fibers are shown in **Figure 4.11** and **Figure 4.12** respectively. These are not substantially different from that of the 200 °C sample.

The interfacial behavior changes substantially after the pyrolysis at 800 °C. The fragmentation length-to-diameter ratio decreases substantially to the level seen for the uncoated fiber (i.e. 53) and remains low (i.e. 59) after the 1000 °C pyrolysis. This corresponds to a much higher degree of adhesion, as the values of the interfacial shear strength of the 800 °C and the 1000 °C treated fibers are 22.60 MPa and 21.28 MPa respectively which are very close to that of the uncoated fiber. The photoelastic stress patterns for the 800 °C and the 1000 °C treated coated fibers (**Figures 4.13 and 4.14** respectively) are also significantly different from those of the coated fibers treated up to 600 °C. Initially at low strains when a fiber has broken, the photoelastic stress patterns are

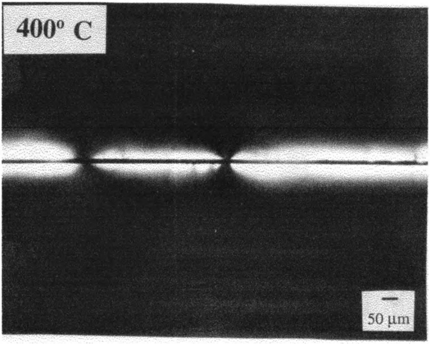

Figure 4.11 Transmitted polarized light photoelastic stress pattern of a 400 °C treated coated carbon fiber under load in the single fiber fragmentation test.

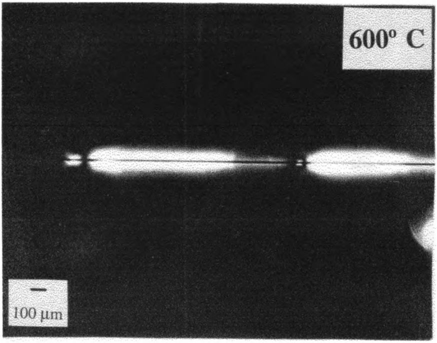

Figure 4.12 Transmitted polarized light photoelastic stress pattern of a 600 °C treated coated carbon fiber under load in the single fiber fragmentation test.

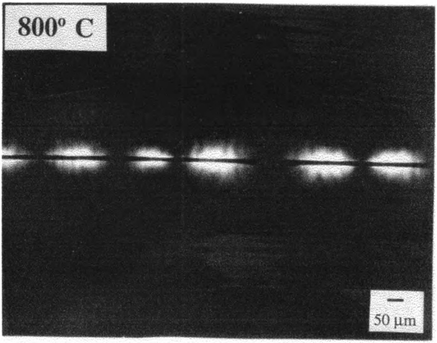

Figure 4.13 Transmitted polarized light photoelastic stress pattern of an 800 °C treated coated carbon fiber under load in the single fiber fragmentation test.

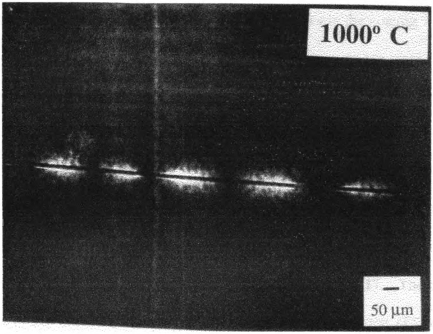

Figure 4.14 Transmitted polarized light photoelastic stress pattern of a 1000 °C treated coated carbon fiber under load in the single fiber fragmentation test.

intense and uniform. At higher strains, however, regular variations in intensity appear perpendicular to the fiber axis. Observation of the coating at higher magnifcations indicates the presence of circumferential cracks in the region near the fiber ends which were not detected in the coatings pyrolyzed at temperatures upto 600 °C. The photoelastic stress patterns and the appearance of cracks in the coating were observed in both the 800 °C and the 1000 °C treated coatings. The cracks are more readily observed in reflected light micrographs of the fibers as shown in **Figure 4.15** (Lines have been added above the fiber to direct the readers' attention to the location of the coating cracks).

4.3.2 ITS Test

The ITS results of uncoated and the coated fibers are shown in **Table 4.4** and a graphical representation is shown in **Figure 4.16**. A typical micrograph of a specimen in the ITS test showing an indented fiber is given in **Figure 4.17**. The interfacial shear strength of the uncoated fiber (i.e. 20.78 MPa) obtained from the ITS test is about the same as that of the fragmentation test in spite of the fact that the two adhesion measurement methods differ substantially in the principle of their operation. The interfacial shear strength values for the coated fibers treated at 200 °C, 400 °C and 600 °C are decreased to about 6.8 MPa from the value of 20.8 MPa for the uncoated fiber. An increasing trend in the interfacial shear strength is there in the 800 °C and the 1000 °C treated coated fibers as the values are 7.1 MPa and 10.8 MPa respectively. The trend of results of the ITS test are similar to those obtained from the fragmentation test. The load versus displacement plot shown in **Figure 4.18** obtained from the ITS test shows a continuous increase in the load until the debond criterion is met in the case of the uncoated

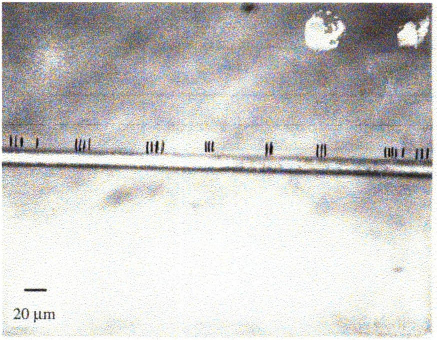

Figure 4.15 Reflected light micrograph of 1000 °C treated fiber with coating fractures indicated by vertical marks.

Table 4.4 Interfacial shear strength (MPa) by the microindentation with the interfacial testing system (ITS).

Uncoated Carbon	200 °C	400 °C	600 °C	800 °C	1000 °C
20.78 ± 0.57	6.87 ± 0.66	6.82 ± 0.72	6.57 ± 0.63	7.09 ± 0.70	10.80 ± 1.06

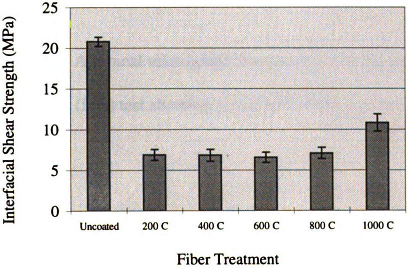

Figure 4.16 Interfacial Shear Strength Determined by the Microindentation with the Interfacial Testing System.

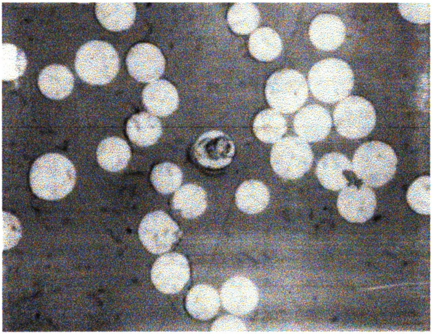

Figure 4.17 A typical micrograph of a specimen in the microindentation (ITS) test showing an indented fiber (in the center).

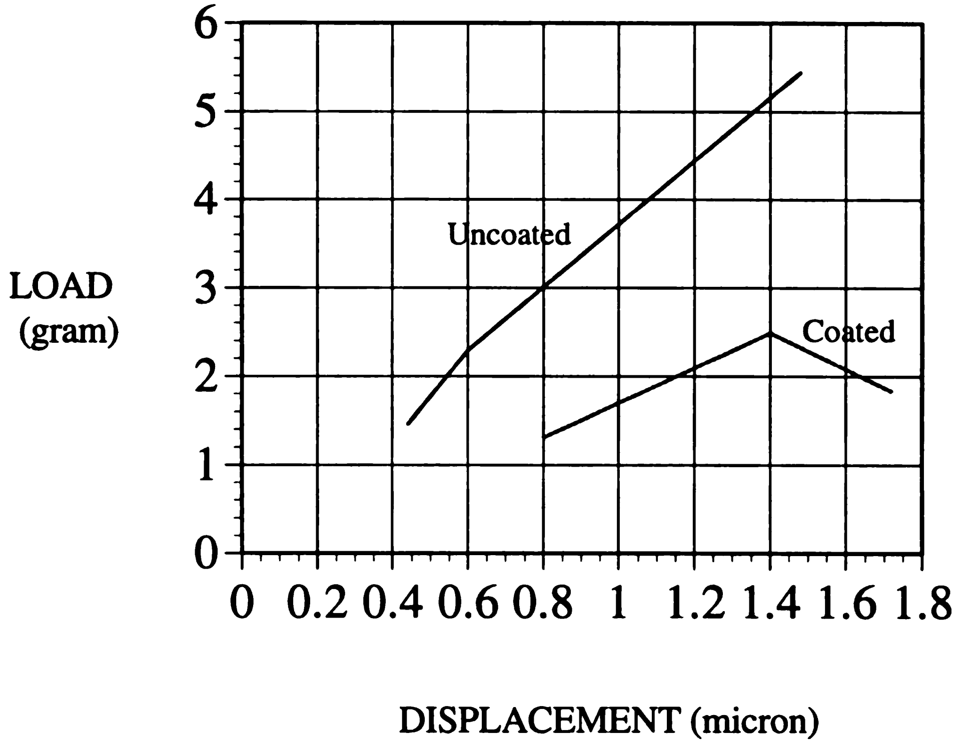

Figure 4.18 Load versus displacement graph of the uncoated and coated carbon fibers obtained from the ITS test.

fibers, whereas, in the case of the coated fibers, a sudden drop in load can be attributed to the low adhesion level between the fiber and the matrix.

4.4 ULTRAMICROTOMY and TRANSMISSION ELECTRON MICROSCOPY

Ultramicrotomy and transmission electron microscopy was done to explore the nature of the interfacial region and to identify the interfacial failure (i.e. fiber-coating failure or coating-matrix failure) in the single fiber fragmentation test's dog-bone coupons.

Transmission electron micrograph of a typical ultramicrotomed section containing an elliptical fiber in the matrix is shown in **Figure 4.19**. The knife direction is shown by the arrow and it is perpendicular to the interface. Note that the fiber is not in the form of a smooth unperforated layer, but it consists of small broken pieces of the graphitic structure. We want to look at the interface between the fiber and the matrix. The results of the ultramicrotomy of the 200 °C, 400 °C, 600 °C, 800 °C and 1000 °C treated coated fibers for both unstrained and strained dog-bone coupons when observed through transmission electron microscope are shown in **Figures** 4.20, 4.21, 4.22, 4.23 and 4.24 respectively. Arrows are drawn in the figures to show the direction of the knife. The direction of the knife is always perpendicular to the interface. In these figures, the unstrained samples of all the treated fibers show that the fiber is very well attached to the matrix. In other words, the interface in the unstrained coupons is intact. Whereas, in the strained samples, the fiber is not well attached to the matrix. This represents a disrupted interface because the sample has been subjected to uniaxial tension which caused an interfacial failure.

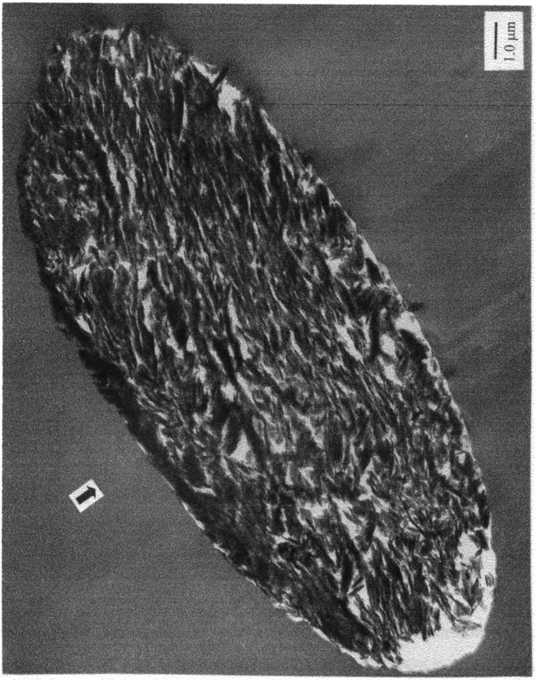

Figure 4.19 Transmission electron micrograph of a typical ultramicrotomed section containing an elliptical shaped fiber in the matrix. The direction of the knife is shown by the arrow and it is perpendicular to the interface.

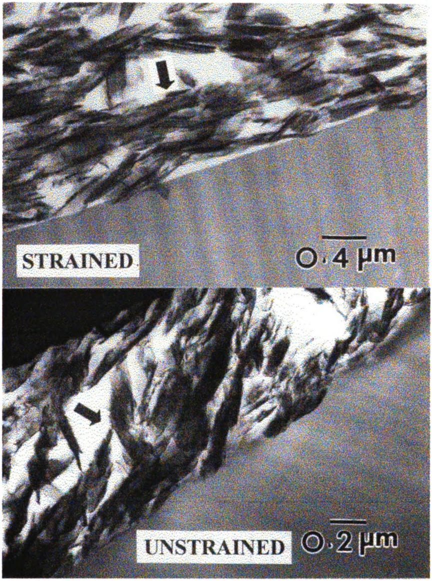

Figure 4.20 Transmission electron micrographs of ultramicrotomed section of 200 °C treated coated fiber obtained from strained (above) and unstrained (below) dog-bone coupons. The direction of the knife is shown by the arrows.

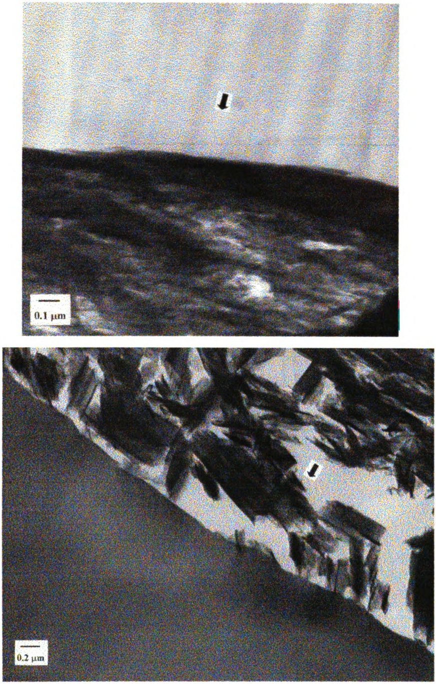

Figure 4.21 Transmission electron micrographs of ultramicrotomed section of 400 °C treated coated fiber obtained from unstrained (above) and strained (below) dog-bone coupons. The direction of the knife is shown by the arrows.

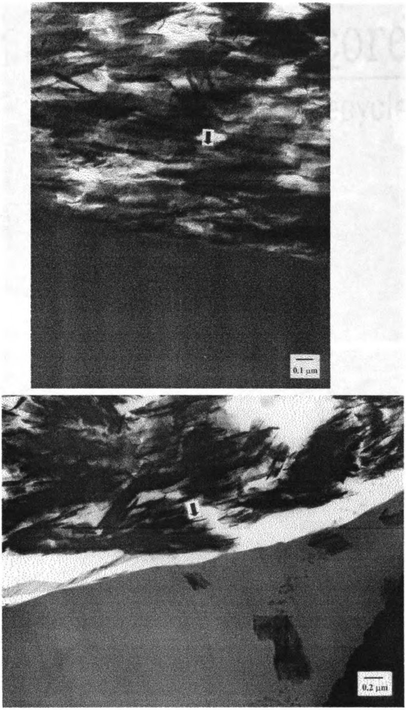

Figure 4.22 Transmission electron micrographs of ultramicrotomed section of 600 °C treated coated fiber obtained from unstrained (above) and strained (below) dog-bone coupons. The direction of the knife is shown by the arrows.

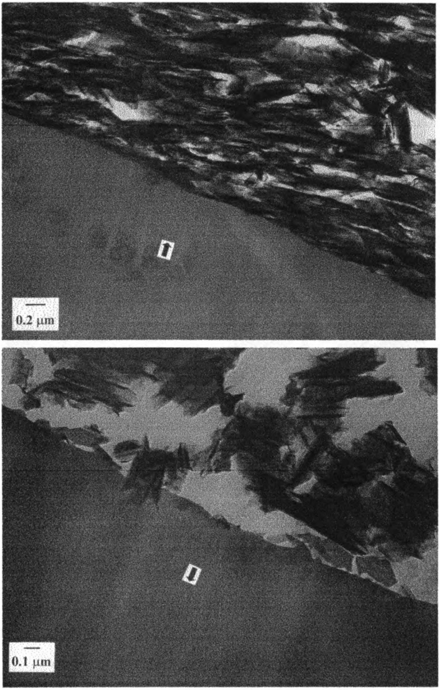

Figure 4.23 Transmission electron micrographs of ultramicrotomed section of 800 °C treated coated fiber obtained from unstrained (above) and strained (below) dog-bone coupons. The direction of the knife is shown by the arrows.

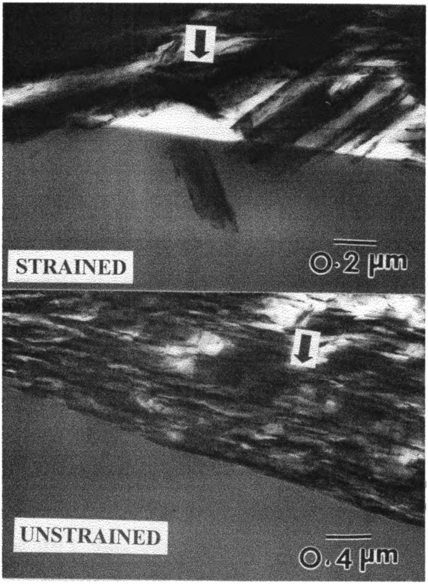

Figure 4.24 Transmission electron micrographs of ultramicrotomed section of 1000 °C treated coated fiber obtained from strained (above) and unstrained (below) dog-bone coupons. The direction of the knife is shown by the arrows.

In case of the sections obtained from the strained coupons (of 200 °C to 1000 °C treated coated fibers), it was observed that a little part from the fiber side (about 0.1 µm) is adhering to the matrix at different spots all around the fiber-matrix interface. **Figure 4.25 and Figure 4.26** show the transmission electron micrographs of ultramicrotomed ssection in which the part from the fiber side is adhering to the matrix in the case of 200 °C and 800 °C treated strained samples respectively. The direction of the knife is shown by the arrow in the micrographs. Since the thickness of the coating is about 0.1µm, the adhering material is the coating of the fiber. Energy dispersive X-ray analysis was done to verify that the material adhering to the matrix side is the coating, i.e., to verify that it contains the coating element (i.e. silicon) in it. Silicon was detected in each of the 200 °C, 400 °C, 600 °C, 800 °C and 1000 °C treated coated and strained fiber's ultramicrotomed section. **Figure 4.27** shows the typical silicon peak obtained in the X-ray analysis of a coated fiber's ultramicrotomed section. An attempt was made to closely observe the ultramicrotomed sections of the strained dog-bone coupons of the 200 °C, 400 °C, 600 °C, 800 °C and 1000 °C treated coated fibers in order to qualitatively determine the amount of the coating adhering to the matrix. The results of this observation are shown in **Figure 4.28**. The 200 °C sample shows about 50%, the 400 °C and 600 °C show about 60%, whereas the 800 °C and the 1000 °C samples show about 75% coating adhering to the matrix. This can be attributed to qualitatively represent the type of interfacial failure i.e. whether the failure is between fiber and coating or between coating and matrix. The 800 °C and the 1000 °C treated strained samples have a greater percent (i.e. 75%) of fiber-coating failure. Therefore, the fiber-coating failure is dominated in the 800 °C and the

Figure 4.25 Transmission electron micrograph of an ultramicrotomed section obtained from the strained dog-bone coupon of 200 °C treated coated fiber showing the coating adhering to the matrix. The direction of the knife is shown by the arrow.

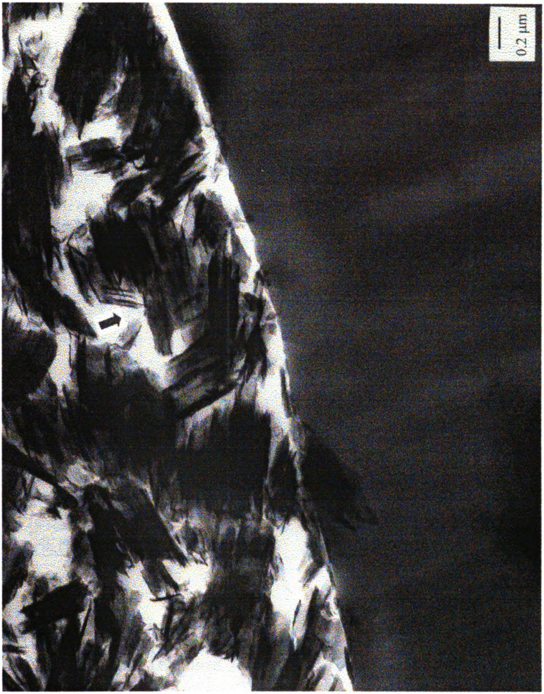

Figure 4.26 Transmission electron micrograph of an ultramicrotomed section obtained from the strained dog-bone coupon of 800 °C treated coated fiber showing the coating adhering to the matrix. The direction of the knife is shown by the arrow.

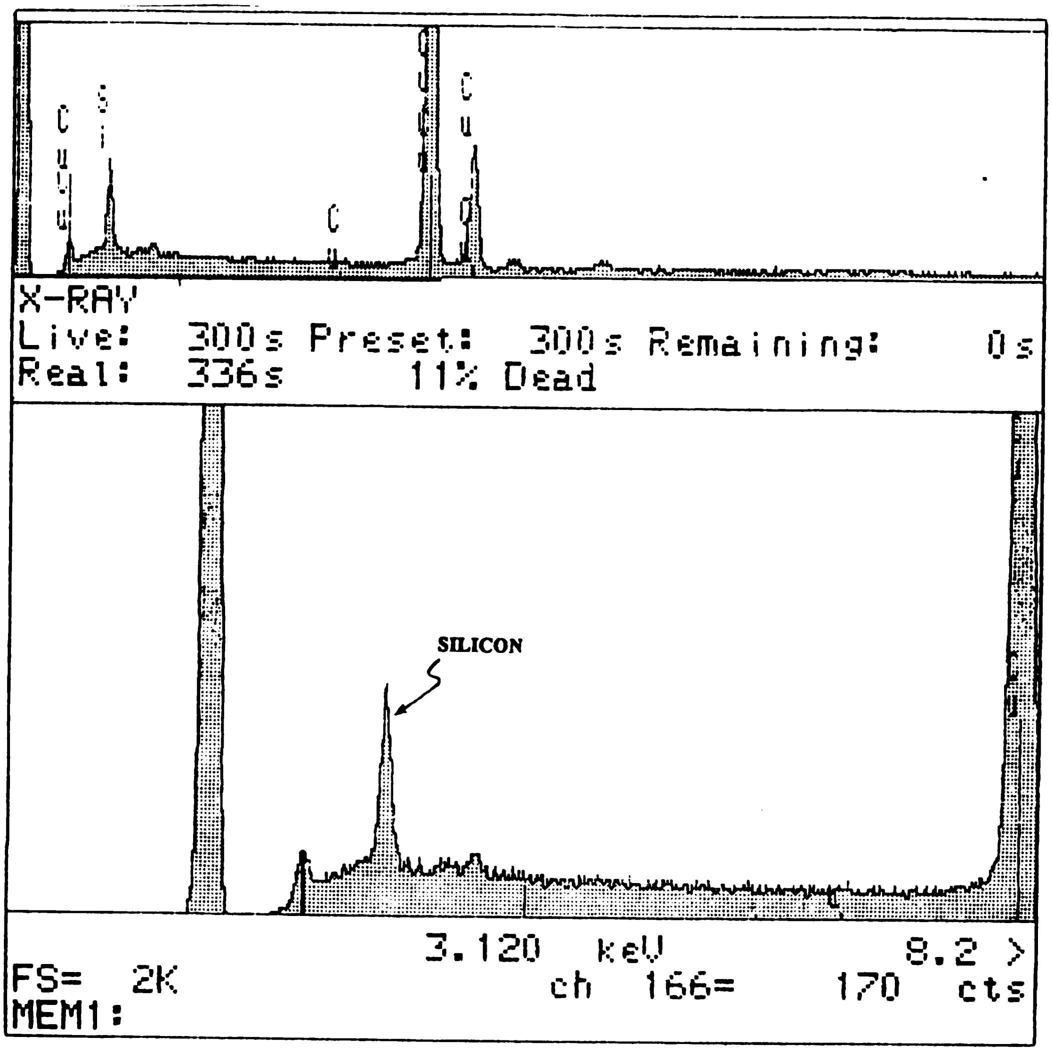

Figure 4.27 Typical graph showing the presence of silicon (adhering to the matrix) obtained in the energy dispersive X-ray analysis of ultramicrotomed section from a coated fiber's strained dog-bone specimen.

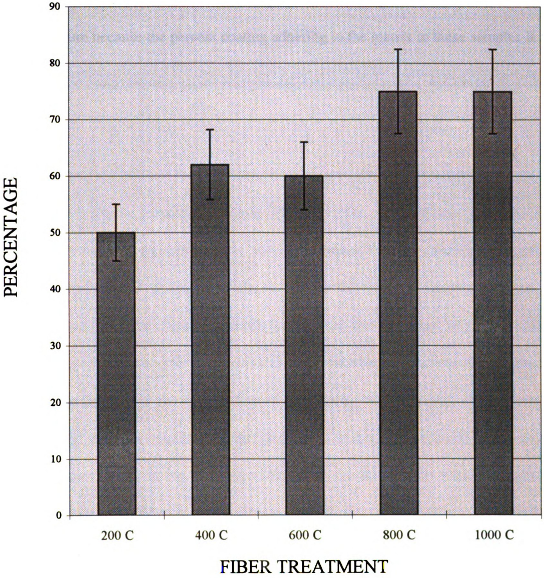

Figure 4.28 Percentage of the coating adhering to the matrix in the ultramicrotomed sections from strained dog-bone specimens of 200 °C to 1000 °C treated fibers observed through the transmission electron microscope.

1000 °C treated coated fibers. The 200 °C, the 400 °C and the 600 °C treated strained samples can be said to have been failed by both the coating-matrix failure and the fiber-coating failure because the percent coating adhering to the matrix in these samples is 50%-60%.

CHAPTER 5

FINITE ELEMENT MODEL and DISCUSSION

When the fiber heat treatment temperature increases, the preceramic coating on the fiber converts from a polymer to a more brittle ceramic. The modulus (and perhaps the strength) of the coating increases as the heat treatment temperature gets higher. In addition, as a result of the mass loss due to the elimination of the starting monomer units at high temperature, the coating becomes thinner with increasing temperature. Although, in this case, we are not able to measure directly the coating mechanical properties, the effect of the increase in the temperature of the coating heat treatment on the interphase shear strength can be evaluated through the effect of coating modulus and thickness on the coating stress transfer of the fragmented fiber. A non-linear finite element analysis was used to examine the influence of the coating parameters on the coating stress fields of a single fiber fragmentation specimen.

A schematic diagram of a fiber fragment from the single fiber fragmentation specimen is shown in **Figure 5.1**. The fragment is composed of three concentric cylinders representing the fiber, the coating, and the matrix. Because of axisymmetry of the fiber fragment, only a quadrant of the plane containing the cylindrical axis has been analyzed. The aspect ratio (fiber length:fiber diameter) for the fragment is 126.5. The outer matrix diameter of the model is 10.8 times the fiber diameter, large enough to ensure that the

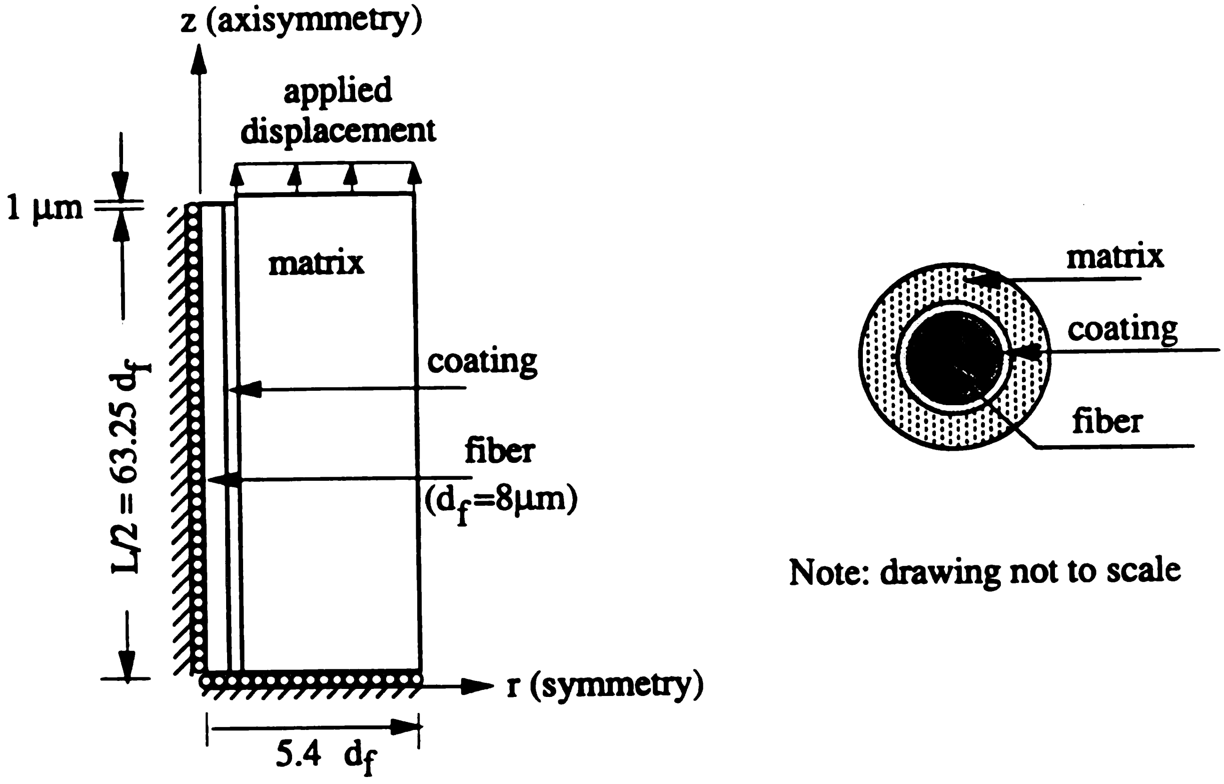

Note: drawing not to scale

Figure 5.1 Finite Element Model.

coating stress-strain transfer is not disturbed by this boundary edge. The fiber diameter used in the model is 8 μm. Along the asymmetric and axisymmetric (fiber center line) axes, roller constraints are applied. A gap length of 2 μm is used in the model to account for the recoil of the fiber when fiber break occurs. It was found that the coating debonding occurs immediately after fiber fracture because of the presence of stress singularities at the fiber breaks **[35,36]**. Thus a debond crack of 20 μm in length along the fiber-coating interface was included in the finite element model. A relative displacement of 8 μm is applied at the upper edge of the model. The effect of the coating thickness on interfacial behavior is evaluated for thicknesses $t_i = 0.0125\ d_f$, $0.05125\ d_f$, $0.125\ d_f$ and $0.25\ d_f$, where t_i and d_f are the coating thickness and fiber diameter respectively. In the system under investigation here with coating thickness of 0.1 μm, the range of coating thickness in the finite element analysis includes this thin layer plus coating layers that are 4, 10 and 20 times as thick.

5.1 MATERIAL PROPERTIES

The carbon fiber used in this numerical analysis is linearly elastic and transversely isotropic. The matrix Epon 828 epoxy with 14.5 wt.% of mPDA (which is the experimental matrix used in this study), is isotropic and non-linear elastic-plastic. For simplicity, the matrix is assumed to behave perfectly plastically after 6% strain. The material behaviors of the fiber and the matrix are shown in **Figure 5.2** and are well documented in the literature **[37,38]**.

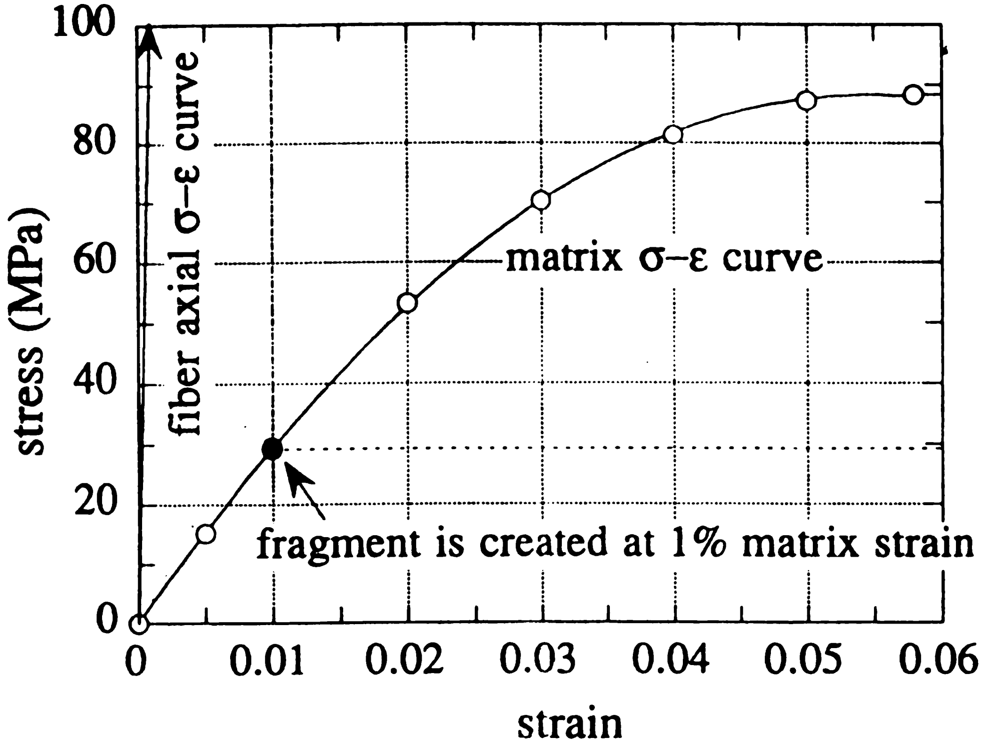

Figure 5.2 Stress-strain curve of the constituent materials.

From experimental observation, it was found that the fiber began to fracture at approximately 0.8%-1% coupon strain in the single fiber fragmentation test. In the model, the fragment is assumed to be created at 1% matrix strain at which point the matrix modulus is lower than it was in the initial non-strained state. The coating property effect is evaluated by varying the coating modulus from that of a compliant polymer coating, e.g. $E_i / E_m = 0.7$, to that of a brittle preceramic polymer coating, e.g. $E_i / E_m = 1.5$, and to that of a more brittle ceramic coating, such as $E_i / E_m = 7.5$ and $E_i / E_m = 30$, where E_i and E_m are the initial coating and matrix moduli respectively.

5.2 NON-LINEAR FINITE ELEMENT ANALYSIS of the EFFECT of COATING MODULUS (200 °C-600 °C)

The fiber axial stress distributions for $E_i / E_m = 0.7$, 1.5, 7.5 and 30 are shown in **Figure 5.3(a)**. It is found that the maximum fiber axial stress (an indicator of stress transfer efficiency) increases about 2% when the coating:matrix stiffness ratio increases from 0.7 to 7.5. The fiber ineffective length (the length within which the fiber axial stress recovers 95% of its far field value) decreases 6.3% when E_i / E_m increases from 0.7 to 7.5. The decrease in the fiber ineffective length with the increasing coating modulus in the numerical analysis corresponds closely to the decrease in the fiber critical length with increasing coating heat treatment temperature from 200 °C to 600 °C in the experimental observation. From the experimental results, it is found that the fiber critical length decreases 18% when the fiber heat treatment temperature increase from 200 °C to 600 °C. Thus the numerical and experimental results show that as the property of the coating on

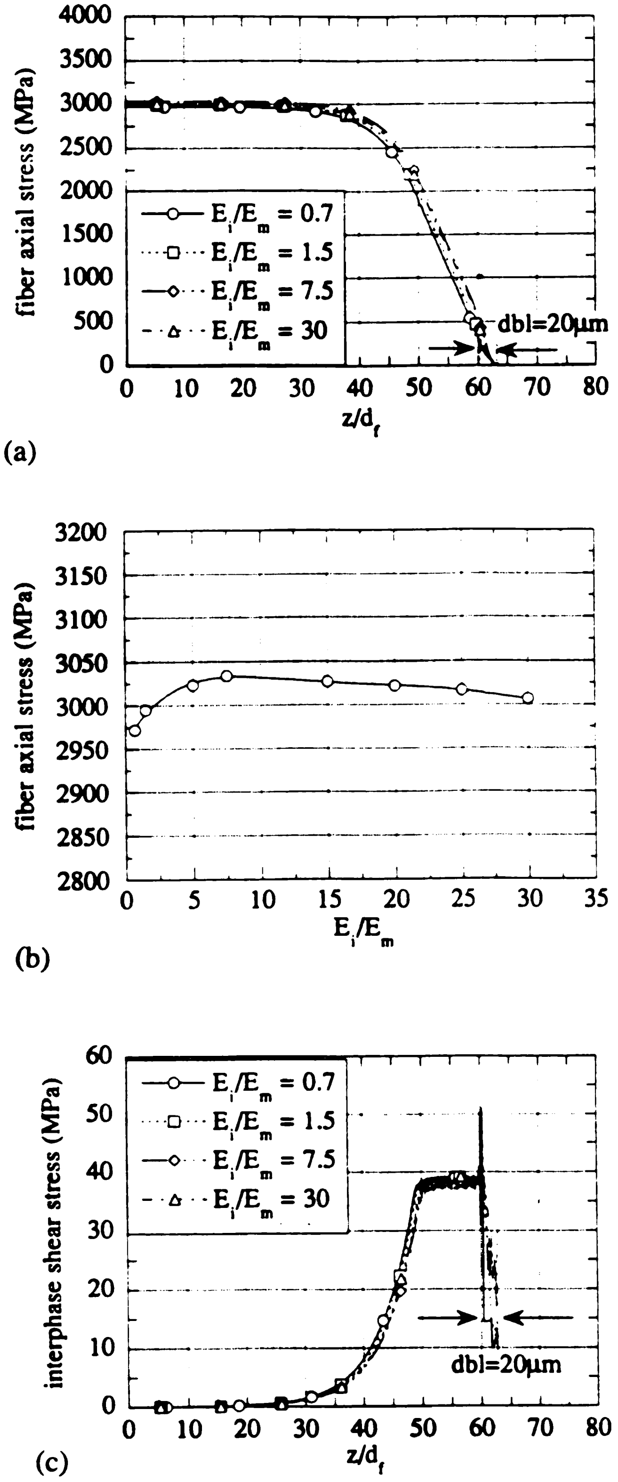

Figure 5.3 (a) Fiber axial and (c) interphase shear stress distributions for fragments with various E_i / E_m ratios; (b) maximum fiber axial stress as a function of E_i / E_m. A 20 μm debond length is assumed at the fiber break.

the fiber improves or as the heat treatment temperature gets higher, the fiber critical length becomes shorter and hence the stress transfer efficiency becomes higher.

However, increasing the coating stiffness does not always increase the stress transfer efficiency. At a certain value of E_i / E_m, the maximum fiber axial stress starts to decrease with increasing E_i / E_m as shown in **Figure 5.3(b)**. In this numerical study, the maximum fiber axial stress for $E_i / E_m = 30$ is less than that for $E_i / E_m = 7.5$ although such a high ratio is not expected to be realistic in this experimental system.

5.3 NON-LINEAR FINITE ELEMENT ANALYSIS of the EFFECT of COATING MODULUS (800 °C-1000 °C)

The experimental results show that there is an abrupt decrease in the critical length when the heat treatment temperature changes from 600 °C to 800 °C. This abrupt change in critical length, however, is not reflected in the finite element analysis. As discussed earlier, the conversion of the coating from polymer to ceramic takes place above 600 °C. Apparently this polymer to ceramic conversion results in a dramatic change in the fiber-coating adhesion as well as the coating properties. However, the level of adhesion and the chemical bond strength have not been incorporated into the finite element model. Nonetheless, the mismatch between the finite element result and the experimental observation indicates that a significant phase change of the coating must have occurred between 600 °C and 800 °C.

The finite element analysis suggests that for fiber coatings treated at 200 °C, 400 °C and 600 °C, the bonding between the fiber and the polymer coating is approximately the same and is not as strong as the bonding between the fiber and the more ceramic coating treated at 800 °C and 1000 °C. This conclusion is supported by the ITS test results. The coating-matrix stiffness ratio is relatively low (less than 7.5). Thus increasing the heat treatment temperature (hence the coating stiffness) increases the stress transfer efficiency (**Figure 5.3(b)**) or decreases the critical length (**Table 4.3**). For the fiber coating treated above 600 °C, the bonding between the fiber and the ceramic coating is much stronger and the debond length is accordingly shorter. As a result, the stress transfer efficiency is much higher and the critical length is much shorter. There is an increase in the coating stiffness as the coating undergoes a phase change from polymer to ceramic. The coating-matrix stiffness ratio is relatively high (above 7.5) but an increase in coating stiffness will result in a decrease in the stress transfer efficiency (**Figure 5.3(b)**). This might explain the increase in the critical length when the coating heat treatment temperature increases from 800 °C to 1000 °C. In addition, the coating tensile stress increases when the coating stiffness becomes higher, which in turn can cause tensile failure of the coating. Hence, the coating will debond as a result of the shear stress concentrations at the coating fractures. This conclusion is supported by the experimental observation of the irregular photoelastic stress patterns and the appearance of the circumferential cracks in the 1000 °C heat treated coating (**Figure 4.15**). Therefore, for the thermal treatment of the fiber coating, a balance between the oxidation resistance (bonding quality) and the material properties has to be achieved.

The shear stress distributions for E_i / E_m = 0.7, 1.5, 7.5 and 30 are shown in **Figure 5.3(c)**. It is found that, near the tip of the debond crack, the shear stress

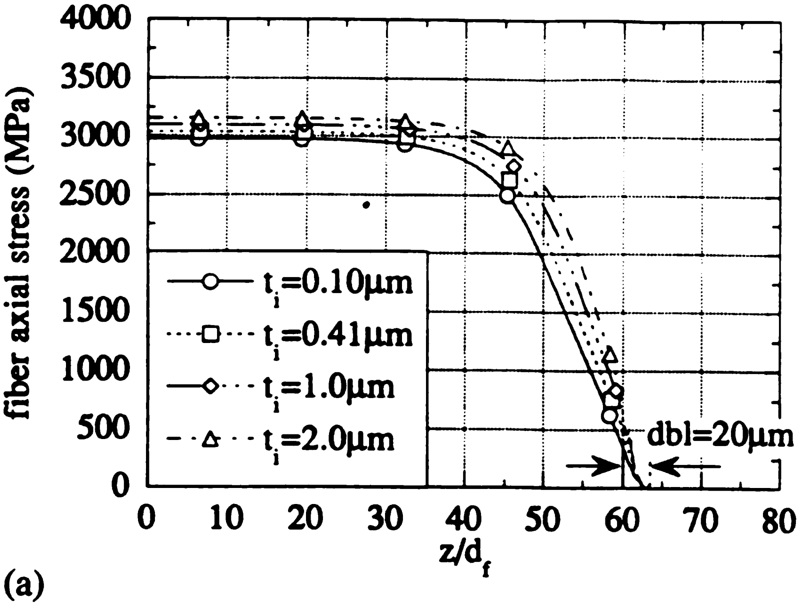

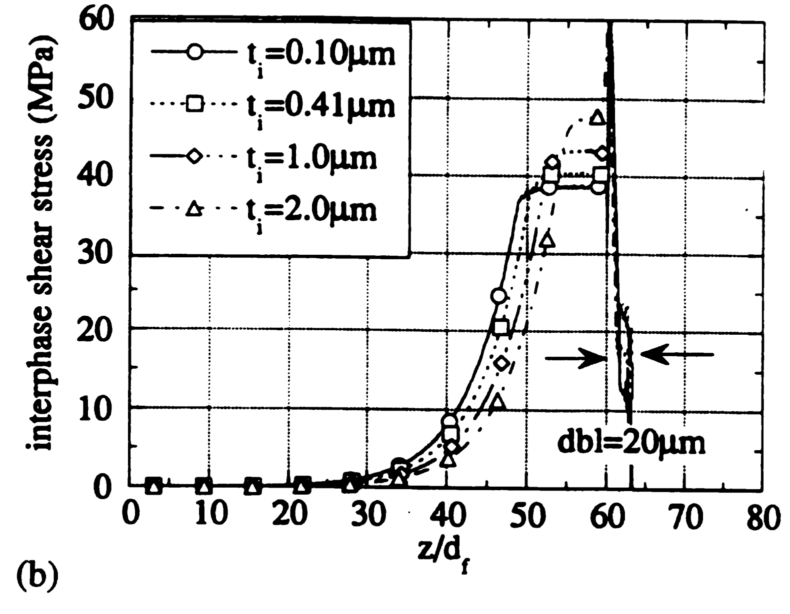

Figure 5.4 (a) Fiber axial and (b) interphase shear stress distributions for fragments with various interphase thicknesses for $E_i/E_m = 1.8$. A 20 μm debond length is assumed at the fiber break.

distributions oscillate with the stress oscillation being greater for the high E_i/E_m case. The shear stress distributions for all cases reach the same plateau as a result of matrix plasticity. It implies that the matrix behavior is a dominant parameter in the coating shear stress transfer.

5.4 EFFECT of COATING THICKNESS

The effect of coating thickness on the coating stress transfer was evaluated for E_i / E_m = 1.8 and E_i / E_m = 0.3. The coating thicknesses t_i studied are 0.0125 d_f, 0.05125 d_f, 0.125 d_f and 0.25 d_f. The fiber axial and coating shear stress distributions for E_i / E_m = 1.8 are shown in **Figure 5.4**. When the coating thickness increases from 0.0125 d_f to 0.25 d_f (an increase of 1900%), the fiber axial stress increases 6% while the shear stress plateau increases 23%. For E_i / E_m = 0.3, when the coating thickness increases from 0.0125 d_f to 0.25 d_f, the fiber axial stress increases 4% (**Figure 5.5(a)**) while the shear stress plateau increases 24% (**Figure 5.5(b)**). Thus the stress transfer efficiency increases with the increase in coating thickness at the expense of increasing the likelihood of shear failure. The stress transfer efficiency increases slightly with a thicker coating for a compliant polymer coating (E_i / E_m < 1) as well as for the more brittle preceramic polymer coating (E_i / E_m > 1). If the change in the coating thickness is not large, the change in the coating stress distribution is marginal. Nevertheless, the coating stress transfer efficiency depends on several factors such as the debond length, the frictional stress between debonded surfaces, the fiber modulus, and the coating modulus and thickness. Overall, the dominant

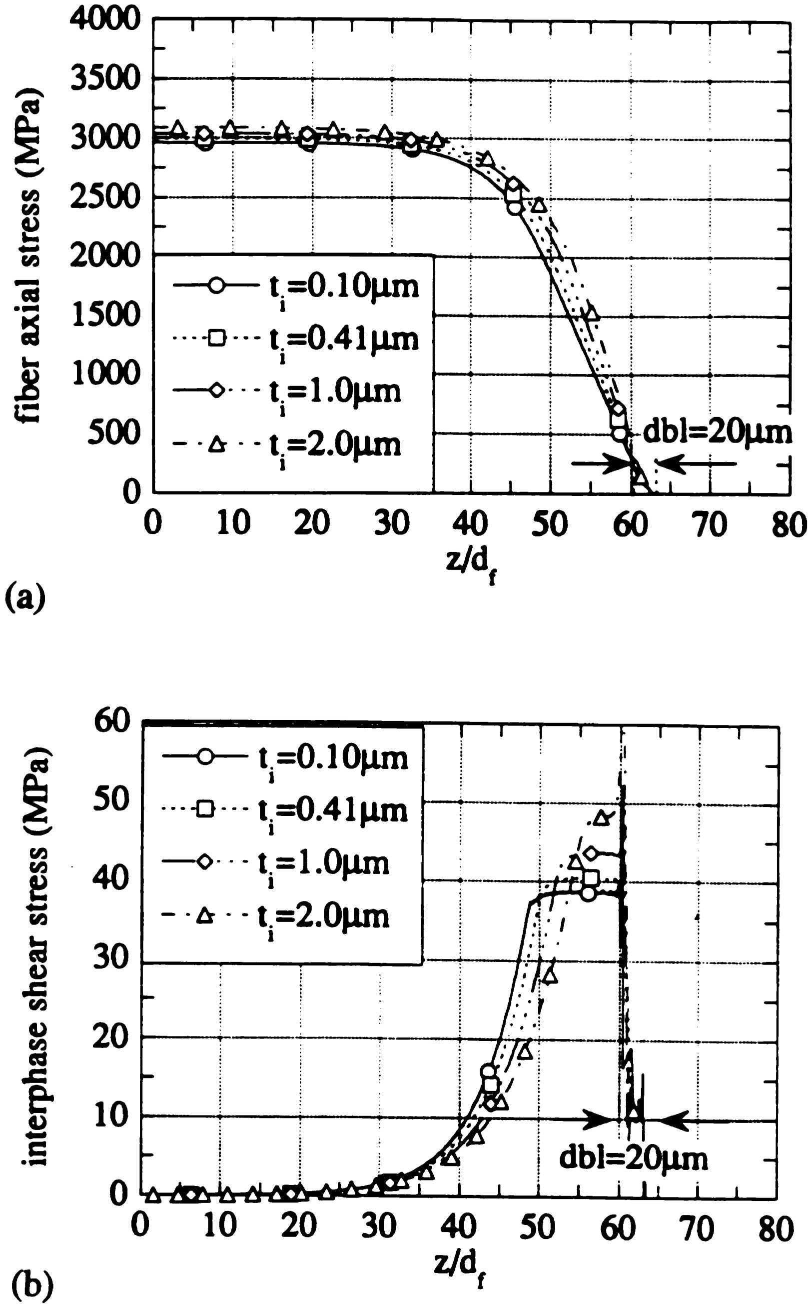

Figure 5.5 (a) Fiber axial and (b) interphase shear stress distributions for fragments with various interphase thicknesses for $E_i/E_m = 0.3$. A 20 μm debond length is assumed at the fiber break.

factor for the coating behavior is the material response of the matrix and the phase of the coating (polymer or ceramic).

CHAPTER 6

CONCLUSIONS

The silsesquioxane coating applied to the graphite fibers by dip coating were shown to form silicon oxycarbide coatings 0.1 μm thick. After pyrolysis in nitrogen to high temperatures (200 °C increments to 1000 °C), amorphous polymeric coatings were shown to convert to amorphous silicon oxycarbide coatings on heating to temperatures above 600 °C.

Single carbon fibers coated with silicon oxycarbide coatings encapsulated in a transparent epoxy matrix exhibited differences in adhesion and fracture behavior as the coating mechanical properties changed with the degree of pyrolysis. Initially the adhesion of the coating in the preceramic inorganic polymer state was low and interfacial failure was observed. After pyrolysis to 800 °C and above, a significant increase in adhesion was detected but the failure mode remained interfacial. Circumferential cracks were detected in the coating. In terms of the locus of interfacial failure, the fiber-coating failure was dominated in the 800 °C and 1000 °C treated strained samples and a mixed fiber-coating and coating-matrix failure was observed in the samples pyrolyzed up to 600 °C. The interface is observed as intact in the case of the unstrained single fiber samples, whereas it is disrupted in the samples subjected to uniaxial tension.

A non-linear axisymmetric finite element model of the single fiber coated material having properties varying in a manner similar to the coating was used to analyze the mechanical state of stress in the coating and at the interface. It was shown that changes in coating thickness had little effect on the critical length-to-diameter ratio. Increase in coating modulus in the model produced interfacial behavior which correlated well with the observed experimental adhesion and interfacial failure results.

BIBLIOGRAPHY

BIBLIOGRAPHY

1. M. Harris, T.M. Chaudhry, L.T. Drzal and R.M. Laine, "Silicon oxycarbide coatings on graphite fibers", Part I. Chemistry, processing and oxidation resistance, Materials Science and Engineering A, 195 (1995) p 223-236.
2. Rosen, B.W., A simple Precedure for Experimental Determination of the Longitudinal Shear Modulus of Unidirectional Composites, *J. Comp. Mater. 6*, 552-4 (1972).
3. J.M. Whitney and L.T. Drzal, Axisymmetric Stress Distribution Around An Isolated Fiber Fragment, *Toughened Composites, ASTM STP 937*, 179-96 (1987)
4. L.J. Broutman and B.D. Agarwhal, A theoretical study of the effect of an interfacial layer on the properties of composites, *Polym. Eng. Sci., 14* (1974) 581-588.
5. E. Plueddermann, *Silane Coupling Agents*, Plenum, New York, 1982.
6. E. Fitzer, K-H. Geigl, W. Huttner and R. Weiss, *Carbon, 18*, (1980) 389.
7. L.T. Drzal, M.J. Rich, M.F. Koenig and P.F. Lloyd, Adhesion of graphite fibers to epoxy matrices. II The effect of fiber finish, *J. Adhes., 16* (1983) 133-152.
8. L.T. Drzal, The effect of polymeric matrix mechanical properties on fiber-matrix interfacial shear strength, *Mater. Sci. Eng. A*, 126 (1990) 289-293.
9. L.T. Drzal and M. Madhukar, "Fibre-Matrix Adhesion and its Relationship to Composite Mechanical Properties", J. Mater. Sci., 28, (1993) p 569-610.

10. L.T. Drzal, M. Madhukar and M.C. Waterbury, Adhesion to carbon fiber surfaces: surface chemical and energetic effects, *Composite Struct., 26* (1993).
11. Drzal, L.T., and P.J. Herrera-Franco, *Composite Fiber-Matrix Bond Tests, Engineered Materials Handbook, 3*, 391 (1991).
12. P.J. Herrera-Franco and L.T.Drzal, "Comparison of Methods for the Measurement of Fibre-Matrix Adhesion in Composites", Composites, Vol. 23, Number 1, 1992, 2-27.
13. A. Kelly and W.R. Tyson, "Tensile Properties of Fiber-Reinforced Metals: Copper/Tungsten and Copper/Molybdenum", J. Mech. Phys. Solids, Vol. 13, 1965, p 329-350.
14. L.T. Drzal, M.J. Rich, J.D. Camping, and W.J. Park, Interfacial Shear Strength and Failure Mechanisms in Graphite Fiber Compsites, Paper 20-C, 35th Annual Technical Conference, Reinforced Plastics/Composites Institute, The Society of the Plastics Industry, 1980.
15. L.T. Drzal, M.J. Rich and P.F. Lloyd, Adhesion of Graphite Fibers to Epoxy Matrices: I. The Role of Fiber Surface Treatment, J. Adhes., Vol 16, 1983, p 1-30.
16. L.T. Drzal, M.J. Rich and M. Koenig, Adhesion of Graphite Fibers to Epoxy Matrices: III. The Effect of Hygrothermal Exposure, J. Adhes., Vol 18, 1985, p 49-72.
17. J.F. Mandell, J.-H. Chen, and F.J. McGarry, "A Microdebonding Test for In-Situ Fiber-Matrix Bond and Moisture Effects", Research Report R80-1, Department of Materials Science and Engineering, Massachusetts Institute of Technology, Feb. 1980.

18. Mandell, J.F., Grande, D.H., Tsiang, T.-H. and McGarry, F.J., "Modified Microdebonding Test for Direct *In Situ* Fiber/Matrix Bond Strength Determination in Fiber Composites", Composite Materials: Testing and Design (Seventh Conference), ASTM STP 893, J.M. Whitney, Ed., American Society for Testing and Materials, Philadelphia, 1986, pp 87-108.

19. (a) M. Harris, in partial fulfillment of Master's Thesis, Department of Materials Science and Engineering, University of Michigan, (1994). (b) M. Harris, C. Scotto, R.M. Laine, unpublished work.

20. R. Baney in "Ultrastructure Processing of Ceramics, Glasses, and Composites", edited by L.L. Hench and D.R. Ulrich, Wiley-Interscience, (1984) p 245-255.

21. D.A. White, S.M. Oleff, R.D. Boyer, P.A. Budringer, J.R.Fox, "Preparation of Silicon Carbide from Organosilicon Gels: I, Synthesis and Characterization of Precursor Gels", Adv. Cer. Mat., (1987) 2, 45-52.

22. D.A. White, S.M. Oleff, J.R. Fox, " Preparation of Silicon Carbide from Organosilicon Gels: II, Gel Pyrolysis and SiC Characterization", Adv. Cer. Mat., (1987) 2, 53.

23. F.I. Hurwitz, L. Hyatt, J. Gorecki, L. D'Amore: "Silsesquioxanes as Precursors to Ceramic Composites", Ceram. Eng. Proc., (1987) 8, 732-43.

24. H. Zhang, C.G. Pantano, "Synthesis and Characterization of Silicon Oxycarbide Glasses", J. Am. Ceram. 73, 958-63 (1990).

25. K. Kamiya, T. Yoko, K. Tanaka, M. Takeuchi, "Thermal Evolution of Gels from $CH_3Si(OC_2H_5)_3$ by the Sol-Gel Method", J. Non-cryst. Sol., (1990) 121, 182-87.

26. G.M. Renlund, S. Prochazka, R.H. Doremus, "Silicon Oxycarbide Glasses: Part I, Preparation and Chemistry", J. Mater. Res. Soc. (1991) 6, 2716.
27. G.M. Renlund, S. Prochazka and R.H. Doremus, "Silicon Oxycarbide Glasses: Part II, Structure and Properties", J. Mater. Res. Soc. (1991) 6, 2723.
28. K. Kamiya, O. Makoto, T. Yoko, J. Noncryst. Sol.; 83, 208 (1986).
29. J.A. Rahn, R.M. Laine, Z-F. Zhang, "The Catalytic Synthesis of Inorganic Polymers for High Temperature Applications and as Ceramic Precursors" in "Polymer Based Molecular Composites", Mater. Res. Soc. Sym. Proc., Vol. 171, D. Schaefer, W. Rhine, eds., (1990) p. 31-38.
30. R.M. Laine, K.A. Youngdahl, F. Babonneau, J.F. Harrod, M.L. Hoppe, J.A. Rahn, "Synthesis and High Temperature Chemistry of Methylsilsesquioxane Polymers Produced by Titaniuim Catalyzed Redistribution of Methylhydridooligo- and polysiloxanes", Chem. Mater. (1990) 2, 464-472.
31. General Electric Company, silicon products department, Waterford, N.Y. 12188.
32. Walls, J.M. (Ed.), "Methods of Surface Analysis", Cambridge University Press, Cambridge, 1989.
33. Einstein, A. (1905), *Annalen der Physik*, 17, 132.
34. Malis, T.F. and D. Steele, "Ultramicrotomy for Materials Science", in Workshop on Specimen Preparation for TEM Materials II, R. Anderson, Ed., Materials Research Society Symposium Proceedings, 199, Pittsburgh, PA, 315 (1990).
35. H. Ho and L.T. Drzal, Non-linear numerical study of the single fiber fragmentation test, part I: test mechanics, *Compos. Eng.*, in press.

36. H. Ho and L.T. Drzal, Non-linear numerical study of the single fiber fragmentation test, part II: a parametric study, *Compos. Eng.*, in press.

37. V.B. Gupta, L.T. Drzal, C.Y.-C. Lee and M.J. Rich, The temperature-dependence of some mechanical properties of a cured epoxy resin system, *Polym. Eng. Sci.*, 25 (1985) 812-823.